

**August 2011**

**Thesis for Master Degree**

# **Simulation of Magneto-Optical Nondestructive Testing**

**Graduate School of Chosun university**

**Department of Control and Instrumentation**

**Engineering**

**Le Minh Huy**

# 자기광학 비파괴검사의 시뮬레이션

**Simulation of Magneto-Optical Nondestructive Testing**

2011년 8월 25일

조선대학교 대학원

제어계측공학과

레민후이

# 자기광학 비파괴검사의 시뮬레이션

지도교수            이 진 이

이 논문을 공학석사 학위신청 논문으로 제출함


2011년 4월


조선대학교 대학원


제어계측공학과

레민후이

# 레민후이의 석사학위논문을 인준함.

위 원 장 조선대학교 교수 趙昌鎭 

위 원 조선대학교 연구교수 全鍾煥 

위 원 조선대학교 교수 李鎭伊 

2011년 5월

조선대학교 대학원

# Contents

초 록.....	iii
<b>ABSTRACT</b> .....	iv
<b>Chapter 1</b> .....	1
<b>INTRODUCTION</b> .....	1
<b>Chapter 2</b> .....	3
<b>PHYSICAL PROPERTIES OF MOF AND ITS MODELIZATION</b> .....	3
<b>2.1. The Faraday effect and Magneto-Optical Sensor</b> .....	3
<b>2.2. The change in the magnetic domains cause by an external magnetic field</b> ....	4
<b>2.3. The saturated magnetization of magneto-optical element</b> .....	5
<b>2.4. Bias of the magnetic field</b> .....	6
<b>2.5. Temperature properties</b> .....	7
<b>Chapter 3</b> .....	9
<b>STATIC MAGNETIC FIELD</b> .....	9
<b>3.1. Horizontal magnetization</b> .....	9
3.1.1. <i>Magnetizers and ANSYS simulation</i> .....	9
3.1.2. <i>Dipole model</i> .....	18
3.1.3. <i>Magneto-Optical Image Processing</i> .....	20
3.1.4. <i>Simulation and experiment results</i> .....	23
<b>3.2. Vertical magnetization</b> .....	27
3.2.1. <i>Magnetizer and ANSYS simulation</i> .....	27
3.2.2. <i>Dipole model</i> .....	32
3.2.3. <i>Magneto-Optical Image Processing</i> .....	33
3.2.4. <i>Simulation and experiment results</i> .....	34
<b>Chapter 4</b> .....	36
<b>ALTERNATIVE MAGNETIC FIELD</b> .....	36
<b>4.1. Model of MOI system and ANSYS simulation of STIC</b> .....	36
<b>4.2. The first suggestion</b> .....	40

4.2.1.	<i>Dipole model</i> .....	40
4.2.2.	<i>Magneto-optical image processing</i> .....	42
4.2.3.	<i>Magneto-optical image processing</i> .....	45
<b>4.3.</b>	<b>The second suggestion</b> .....	47
4.3.1.	<i>Dipole model</i> .....	47
4.3.2.	<i>Results and discussion</i> .....	48
<b>4.4.</b>	<b>The third suggestion</b> .....	49
4.4.1.	<i>Dipole model</i> .....	49
4.4.2.	<i>Results and discussion</i> .....	50
<b>Chapter 5</b> .....		52
<b>CONCLUSIONS</b> .....		52
<b>ACKNOWLEDGEMENT</b> .....		58

# 초 록

## 자기광학 비파괴검사의 시뮬레이션

레 민 후이

지도교수 : 이 진 이

조선대학교 일반대학원 제어계측공학과

금속성 시험편에 인가되는 전자기장의 활용으로부터 얻어지는 전자기장의 결과는 균열의 존재에 의하여 왜곡이 발생한다. 이때, 자기장의 분포는 전자기장에서 발견된 이 왜곡의 결과로서 변화하고, 전자기를 이용한 비파괴검사 방법에서 균열을 검사하는데 사용될 수 있다. 특히, 이 분포는 자기광학 비파괴검사 (MONDI, magneto-optical nondestructive inspection) 시스템을 이용하여 시각화가 가능하다. 평면의 편광된 빛이 자기광학필름 (MOF, magneto-optical film - MONDI의 자기 센서)에 전송 될 때 회전을 하게 되는데, 이는 패러데이 효과(Faraday effect)에 의한 것으로, 일종의 자기광학 효과이다. 그러나, MOF의 자기장 강도는 1 비트의 제한된 분해능을 가지고 있어, 탐상한 결함의 정량적인 평가가 어렵다. 본 논문에서는 자기광학 누설 방법과 자기광학 와전류 탐상법(MOI), 두 가지의 비파괴검사(MONDI)의 시뮬레이션 방법을 보고한다. 이러한 시뮬레이션 방법을 사용함으로써, MOF의 이미지를 추정할 수 있고, 결함을 정량적으로 평가할 수 있다.

# ABSTRACT

## A Non-Destructive Testing Simulation Technique using Magneto-Optical Film

Le Minh Huy

Advisor: Prof. Jinyi Lee, PhD

Dept. of Control and Instrumentation Eng.,  
Graduate School of Chosun University.

An electro-magnetic field resulting from the application of a magnetic or electrical field to a metallic specimen is distorted due to the existence of a crack. The distribution of the magnetic field is changed as a results of this distortion found in the electro-magnetic field, and can be used to inspect crack in the electromagnetic nondestructive testing method. Especially, this distribution can be visualized by using the magneto-optical nondestructive inspection (MONDI) system. The plane of the polarized light beam rotates when the beam is transmitted through the magneto-optical film (MOF - a magnetic sensor in MONDI), caused by the Faraday effect, a kind of magneto-optical effect. However, the MOF has the limited resolution of magnetic field intensity, 1 bit. Correspondingly, the evaluation of inspected crack is difficult. In this paper, the simulation methods of two MONDI, magneto-optical magnetic flux leakage testing and magneto-optical eddy current imager (MOI) are reported. By using these simulation methods, the images on the MOF can be estimated, and the crack can be evaluated quantitatively.

***KEYWORDS: NDT, Crack, Faraday effect, Magneto-Optics, MO film, Leakage Magnetic Flux, Eddy Current.***



# Chapter 1

## INTRODUCTION

Nondestructive Testing (NDT) is very important to ensure the integrity, safety and maintenance of engineering systems. It is widely used in heavy industries such as airplane, power generation, automotive, railway. NDT provides the methods to detect the cracks on specimen without doing harm, stress or destroying the test object. There are many methods used in NDT, some of the most used are Ultrasonic Testing (UT) [1-4], Radiographic Testing (RT) [5-8], Electromagnetic Testing (ET) [9-12], Penetrant Testing (PT) [13-15]. Ultrasonic Testing (UT) uses high frequency sound energy to conduct examination and make measurements. UT system requires the use of a coupling liquid between the transducer and the specimen making test slow and tedious, and also causing contact with the specimen. Radiographic Testing (RT) uses the expensive and cumbersome equipments. The X-ray transmits through the specimen to the receiver which is on the opposite side. So it's complicated to adjust process of the test setup. In addition to being time consuming, RT technique requires specific precaution to avoid radiation hazards. Penetrant Testing (PT) requires liquid penetrant or dry powder applied to surface of specimen, and waiting time. This method is complicated and unable to evaluate the depth of cracks. Electromagnetic Testing (ET) is getting wide interest since it is faster, easier in implementation and offers safety. ET is the process of inducing electric currents or magnetic fields or both inside a specimen and observing the electromagnetic response. There are some common methods of electromagnetic testing such as: Magnetic Particle Testing (MPT), Magnetic Flux Leakage Testing (MFLT) and Eddy-Current Testing (ECT).

The ET in NDT technique has been used for investigation and evaluation of cracks on metallic specimen by the easy and fast implementation method. There are two several common kind of sensors such as Hall sensor (magnetic resistance MR) [16-18] and giant magnetic resistance (GMR) sensor [19-21] which have been used. Another kind of sensor is magneto-optical (MO) sensor [22-24] which uses the Faraday Effect, a kind of magneto-optical effect. The plane of the polarized light beam is rotated when it passes through a magneto-optical film (MOF) in MO sensor such as a bismuth doped iron garnet film. The MOF has a wide area with

high spatial resolution of magnetic domains, so it is possible to inspect with high speed and automated real-time method.

Evaluation of crack such as the direction, size and shape from obtained magnetic field distribution is necessary to determine the time for maintenance. A finite element method (FEM) can be used to calculate the magnetic field. In which, the crack size, the magnetic source, cracks and air are divided into small elements and nodes, and the simultaneous equations of the electro-magnetic field at each element are solved in the FEM [25-29]. Consequently, this method is complex and takes long time of simulation according to the accuracy. Another method is using dipole model (DM) [30-34], which assumes the dipoles magnetic charge are appeared some where on cracks when the magnetic field is applied to the metallic specimen. When static magnetic field is applied to the specimen, the crack is considered to be filled by dipoles with dipole moments oriented opposite to the direction of the applied field. However, the static magnetic field just can be used to detect cracks on ferromagnetic material specimen. With paramagnetic material, we need to use alternative magnetic field which induced eddy current on specimen. When apply alternative magnetic field to specimen, we suggest the dipoles magnetic charge basically appear at the both tips of the crack in which dipoles moment are perpendicular with applied magnetic field direction. Thus, the magnetic field of a point outside of specimen is the sum of the magnetic fields generated by these dipoles. Also, we provide simulation software which is integrated the properties of MOF. To verify our suggestion, I compared the simulation results with experimental results which are obtained by MOI (Magneto-optical/eddy current imager, by PRI Co.).

The thesis has five chapters. The first chapter is introduction chapter. The second chapter describes the physical properties of MOF. The third chapter discusses about the simulation of static magnetic field. The forth chapter discusses about the simulation of alternative magnetic field. The last chapter gives the conclusions.

## Chapter 2

### PHYSICAL PROPERTIES OF MOF AND ITS MODELIZATION

#### 2.1. The Faraday effect and Magneto-Optical Sensor

The Faraday effect, a magneto-optical effect, is the interaction between light and magnetic field in a medium. When the polarized light beam is transmitted through a film (Magneto-Optical Film, MOF), the polarized plane of the light is rotated by an angle called the Faraday angle as shown in Fig. 2-1(a). This angle is proportional to the Verdet constant  $V$ , intensity of magnetization  $B$ , and the thickness of MOF  $t$ , as described by the equation (2-1) [35, 36]:

$$\theta_F = V B t \quad (2-1)$$

L-rotation (anticlockwise) when the direction of propagation and magnetic field are parallel.

R-rotation (clockwise) when the direction of propagation and magnetic field is anti-parallel.

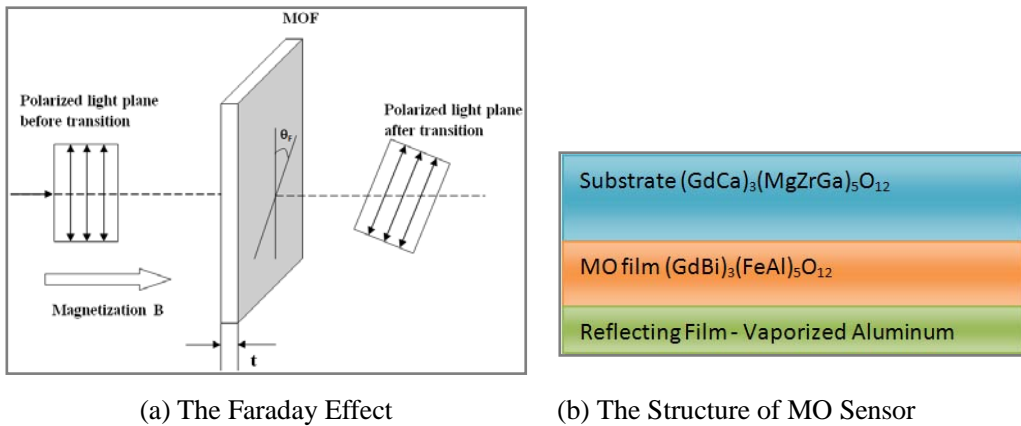


**Fig. 2-1** The Faraday Effect and structure of MO sensor

An MO sensor contains an MO film  $(\text{GdBi})_3(\text{FeAl})_5\text{O}_{12}$ , which is grown on a substrate  $(\text{GdCa})_3(\text{MgZrGa})_5\text{O}_{12}$  and a vaporized aluminum reflecting film as shown in the Fig. 2-1(b). The Faraday rotation is almost doubled in this reflection-type optical system [37]. These films

exhibit three important physical properties of MO sensor. Firstly, they have magnetic anisotropy property, that they have an easy axis of magnetization normal to the sensor surface. Secondly, if the magnetic fields along the easy axis of magnetization are removed, the magneto-optic film will retain most of its established magnetization, that is a memory. Thirdly, these film possess a very large specific Faraday rotation, Faraday angle is up to 30,000 degrees/cm of thickness [38].

## 2.2. The change in the magnetic domains cause by an external magnetic field

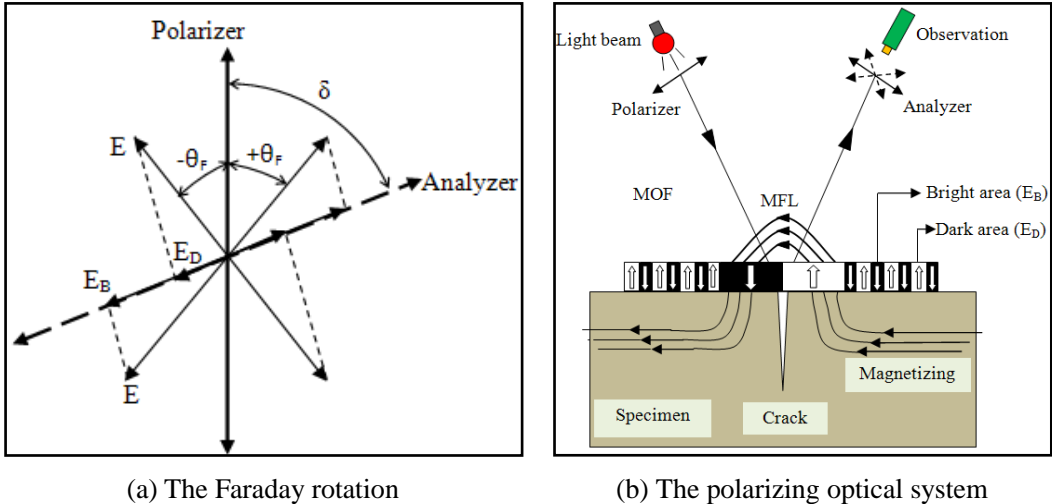


Fig. 2-2 The effect of MOF

The rotation angle and the direction of the Faraday angle are affected by the strength and direction of magnetization as indicated by equation (2-1). Usually, Verdet constant,  $V$  and thickness of MOF,  $t$  are constants. Therefore, the strength and direction of the magnetization can be estimated by estimating the rotation angle. In addition, the magnetic domains of an MOF have only two directions, vertical, up and down to the plane of the MOF because of magnetic anisotropy. Therefore, the polarized light beam is rotated at a clockwise angle ( $\theta_F$ ) and anticlockwise angle ( $-\theta_F$ ) as shown in Fig. 2-2(a). Then the Analyzer obtains the electrical

field of the light  $E_B = E \cos(\delta - \theta_F)$  and  $E_D = E \cos(\delta + \theta_F)$ , where  $E$  is the electrical field of the transmitted light, and  $E_B, E_D$  are the electrical fields of  $+\theta_F$  and  $-\theta_F$ , respectively, and  $\delta$  is the angle between the polarizer and analyzer (Fig. 2-2(b)). Since  $E_B > E_D$ , the MOF has alternating bright areas and dark areas. If there are no cracks on a specimen, the ratio of the bright area and dark area would be the same; if there are cracks on a specimen, the magnetic field around the cracks would be different from that in no-crack area, so the domain widths are changed. Therefore, cracks can be observed by using a polarizing optical system (Fig. 2-2(b)). Also, the domain width of a MOF is approximately 3-50  $\mu\text{m}$  without a magnetic field, which means smaller cracks can be detected by using smaller magnetic domain widths of an MOF.

### 2.3. The saturated magnetization of magneto-optical element

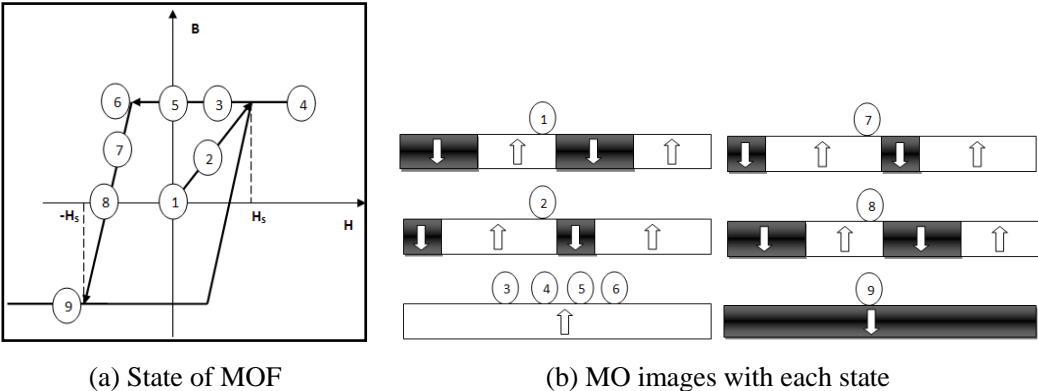


Fig. 2-3 The saturated magnetization effect

As mentioned in the structure of an MOF, the MOF has a reflecting film which reflects the light from the polarizer. The reflected light will form an image on the MOF, including black and white colors according to the intensity of the reflected light. The intensity can be described by the following equation which describes the ratio of bright area and dark area [37]:

$$I = \frac{1}{2} \left[ \frac{Hs + H}{Hs} E^2 \cos^2(\delta - \theta_F) + \frac{Hs - H}{Hs} E^2 \cos^2(\delta + \theta_F) \right] \tag{2-2}$$

where  $H(<|H_s|)$ ,  $H_s$ ,  $E$ ,  $\delta$ ,  $\theta_F$  are the external magnetic flux intensity, the saturated magnetic intensity of the MOF, the electric field of the transmitted light, the angle between the polarizer and analyzer, and the Faraday rotation angle, respectively. Eq. (2) can be expressed in the terms of two functions  $C_1(\delta)$  and  $C_2(\delta)$  [33]:

$$I = C_1(\delta) + C_2(\delta)H \quad (2-3)$$

$$\text{with } C_1(\delta) = \frac{1}{2}E^2[\cos^2(\delta - \theta_F) + \cos^2(\delta + \theta_F)]$$

$$\text{and } C_2(\delta) = \frac{1}{2H_s}E^2[\cos^2(\delta - \theta_F) - \cos^2(\delta + \theta_F)]$$

Equation (2-3) is a linear equation with respect to  $H$  when  $\delta$  is fixed. As shown in Fig. 2-3, if there is no magnetic field ( $H=0$ , case ①) then the width of dark and bright domain are equal (case ②),  $I$  increases, and then, the width of the bright domain increases, and the width of the dark domain decreases. When  $H=H_s$  (saturation, cases ③, ④, ⑤, ⑥),  $I$  is maximum,  $I = E^2\cos^2(\delta - \theta_F)$  and there is only the bright domain. When the direction of  $H$  changes from zero (case ⑦), due to the residual magnetic field ( $B$  decrease,  $B > 0$ ),  $I$  decreases, the width of the bright domain decreases, and the width of the dark domain increases. When  $B=0$  (case ⑧), as in case ①, the dark and bright domain are equal. In the case of ⑨ ( $B < 0$ ,  $H = -H_s$ ), the direction of magnetic field is inversed, and  $I$  is minimum,  $I = E^2\cos^2(\delta + \theta_F)$ . There is only the dark domain.

## 2.4. Bias of the magnetic field

Fig. 2-4 shows the magnetic field without bias magnetic field (the dotted line) and magnetic field with bias magnetic field (the solid line). With bias magnetic field, the total magnetic field is the sum of magnetic fields. The MO sensor responds and forms an image only if the magnetic flux density exceeds a certain threshold value,  $B_s$ , which is a characteristic of the sensor. The bias magnetic field permits adjustments to the MO sensor threshold and optimizes the sensor response to varying field strengths. This bias magnetic field is controlled

by direct bias current, so it's easy to control the level of sensor threshold. Fig. 2-5 shows the experiment results with hole type cracks using an MOI system. When we applied a (-)bias magnetic field, more accurate information about the cracks was obtained than when we had applied a (+)bias magnetic field. In addition, magnetic field background noises such as the earth's magnetic field affected the quality of the MO sensor. Using a bias magnetic field, it was easy to reduce this background noise effect. Therefore, the sensitivity of the MO sensor can be adjusted by using bias magnetic field.

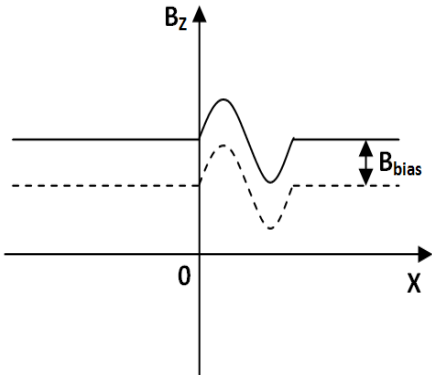


Fig. 2-4 Bias magnetic field

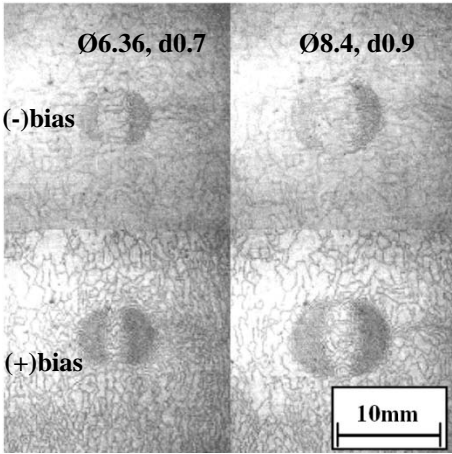
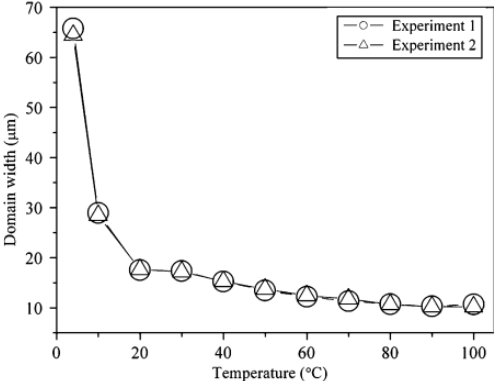


Fig. 2-5 The change of MOF threshold using bias magnetic field

### 2.5. Temperature properties

The NDT technique that can detect a natural crack in the high-temperature testing regime using an MOF was proposed [39]. Also, the behaviors of MOF in the low temperature regime have been studied. As shown in the Fig. 2-6, the domain width increases rapidly in the low temperature areas; therefore, the spatial resolution of MOF is decreased at low temperature. However, the spatial resolution of MOF is increased at high temperatures when the domain width is small. Fig. 2-7 shows the relation between the domain ratio and magnetic flux density for each temperature regime. The domain ratio is the ratio of bright and dark areas, which is approximately 50% without magnetic induction at room temperature. The expansion of the

bright area or the increase of the domain ratio attributed to their linear relation with the increase of magnetic induction. The domain ratio rapid changes at the low temperature regime, so an MOF can saturate easily just with small magnetic induction at low temperatures. It means that an MOF has high sensitivity at low temperature. For a paramagnetic metal specimen with small crack, the distortion of the magnetic field around the cracks is small, so they would have to be detected at low temperatures. The domain ratio changes at around the boiling point of water in Fig. 2-7. Therefore, the cracks on a specimen at several hundred degrees centigrade can be detected using an MOF submerged in distilled water near the boiling point. Then, the crack can be evaluated using the MOF at any temperature.



**Fig. 2-6** Average domain width depends on temperature

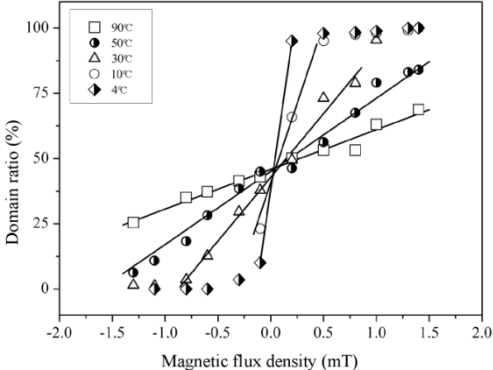


**Fig. 2-7** Domain ratio due to the magnetic flux density



# Chapter 3

## STATIC MAGNETIC FIELD

### 3.1. Horizontal magnetization

#### 3.1.1. Magnetizers and ANSYS simulation

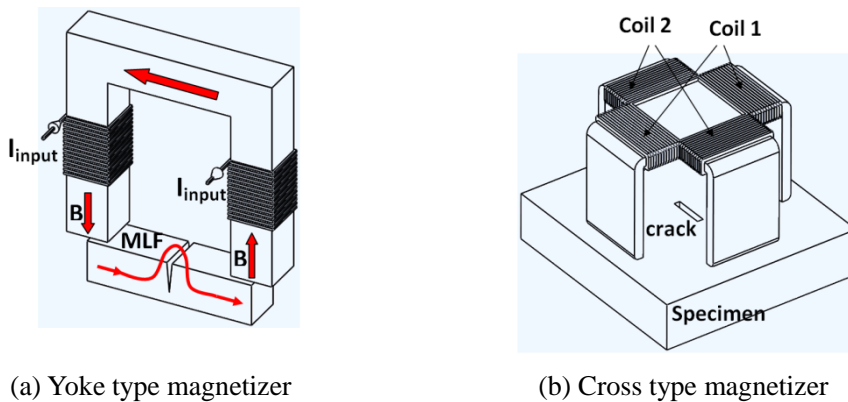
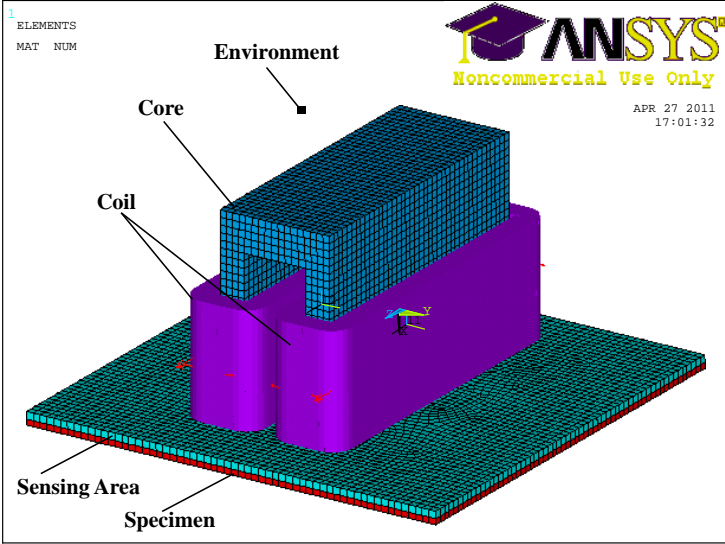


**Fig. 3-1** Model of horizontal magnetization

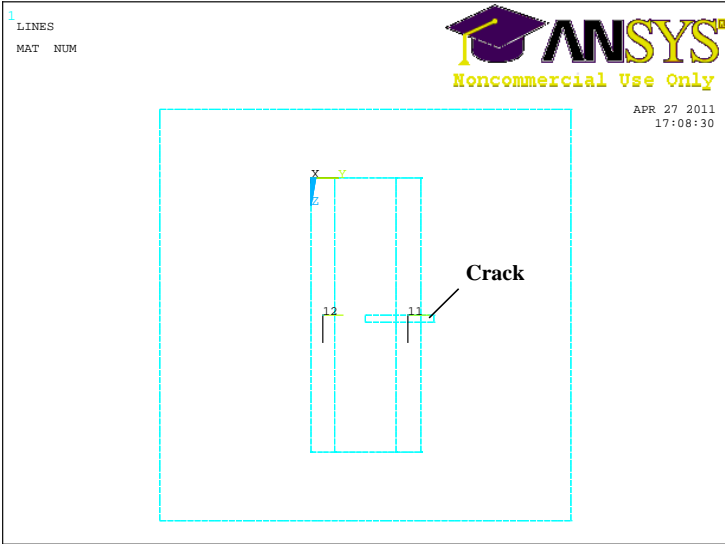
Fig. 3-1(a) shows the model of yoke type magnetizer which has two coils with the inverse input direct current [40]. Magnetic flux is occurred horizontally to the surface of specimen by placing a ferromagnetic specimen at each end of poles. The MFL is appeared due to the existence of cracks. Because of large MFL around crack, the magnetic domains have larger area than those in no-crack area. If the length of crack is parallel with the magnetic direction, the MFL is small and the inspection of crack is difficult. In this case, cross type magnetizer is a good solution (Fig. 3-1(b)). Cross type magnetizer includes of two coils (coil 1, coil 2) which induce two magnetic perpendicularly each other [42]. When doing experiment, we switch input current to each coil and then crack with any direction can be detected.

I analyzed the performance of these magnetizers by FEM using ANSYS program (Ver. 11.0 SP1 UP20070830, EMAG).

*Yoke type magnetizer:*



(a)



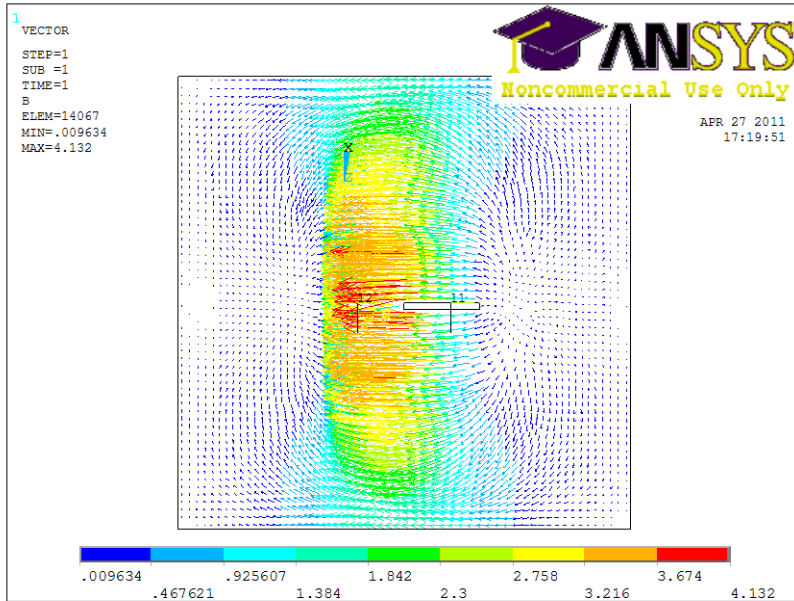
(b)

**Fig. 3-2** Model of system using in ANSYS in the case of yoke type magnetizer  
(a) 3-D model, (b) 2-D view

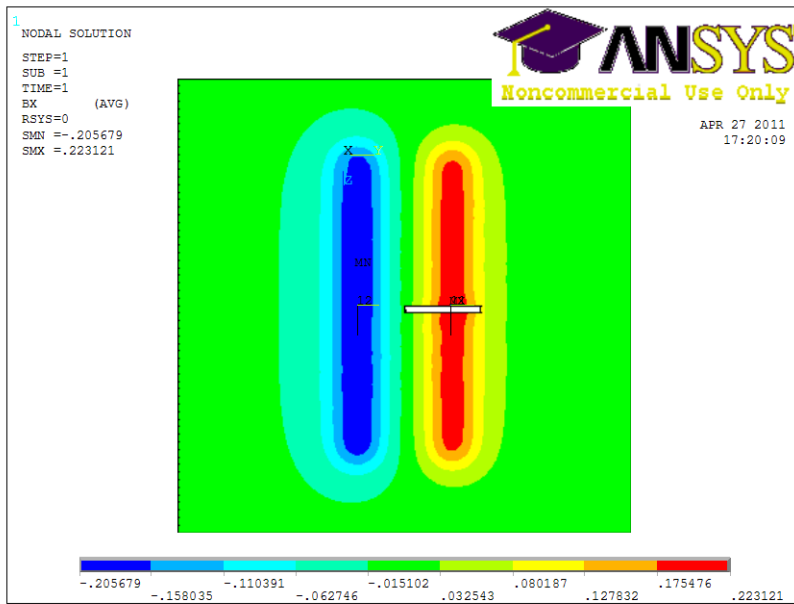
**Table 3-1** Properties of equipments using in ANSYS in the case of yoke type magnetizer

<b>Item</b>	<b>Material</b>	<b>Magnetic properties</b>	<b>Size (mm)</b>	<b>Meshing size (mm)</b>	<b>ANSYS model type</b>
Specimen	Steel	MURX 4000 RSVX 8e-6	60 × 60 × 0.8	1	SOLID117
Core	Mu-metal	MURX 250 RSVX 1.6e-7	16 × 40 × 27	1	SOLID117
Coil	Copper	MURX 1	9.7 × 47 × 16 2 coils x 200 turns x 4.08 A	1	SOURCE36
Sensing area	Air	MURX 1	60 × 60 × 1	1	SOLID117
Crack	Air	MURX 1	1 × 10 × 1	1	SOLID117
Environment	Air	MURX 1	74 × 80 × 42	5	SOLID117

Fig. 3-2 shows the model of system using in ANSYS with the yoke type magnetizer, and the size, others information in the Table 3-1. The yoke type magnetizer has the one core and the two coils which were applied the currents with the different direction each other. On the specimen, there is the sensing area in which the sensor will be located in. All the system was located in the air environment which has the shape of rectangular cuboid. Fig. 3-3 and Fig. 3-4 show the simulation results with the horizontal crack and vertical crack, respectively. In the case of horizontal crack, the distribution of magnetic field around crack was weak. Thus, the sensor will be difficult to inspect this crack. Inversely, the distribution of magnetic field around the vertical crack was stronger than it in no-crack area. Then, the crack will be inspected easily.

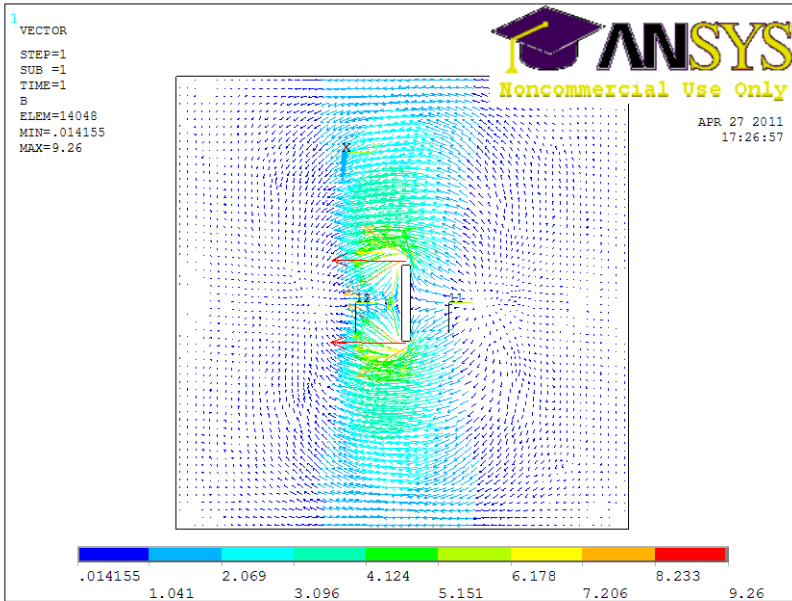


(a)

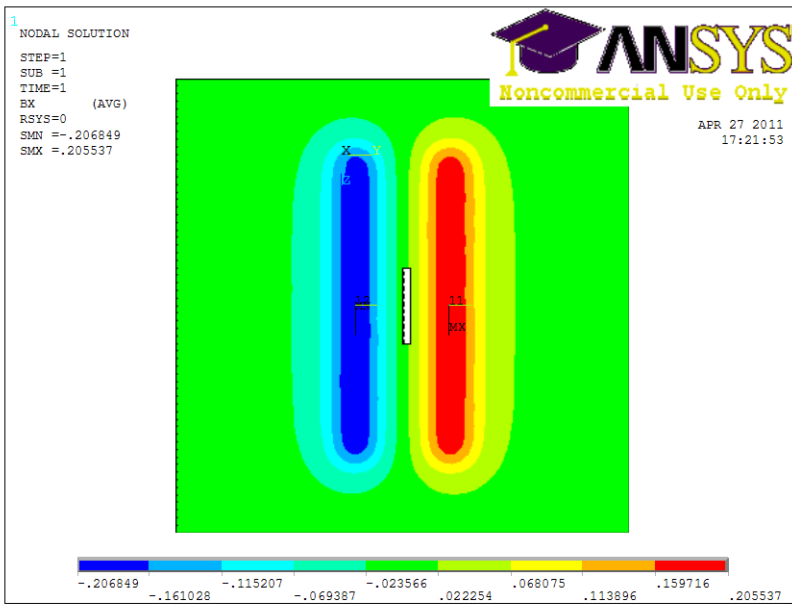


(b)

**Fig. 3-3** Distribution of magnetic density in specimen with horizontal crack using yoke type magnetizer. (a) vector solution, (b) nodal solution



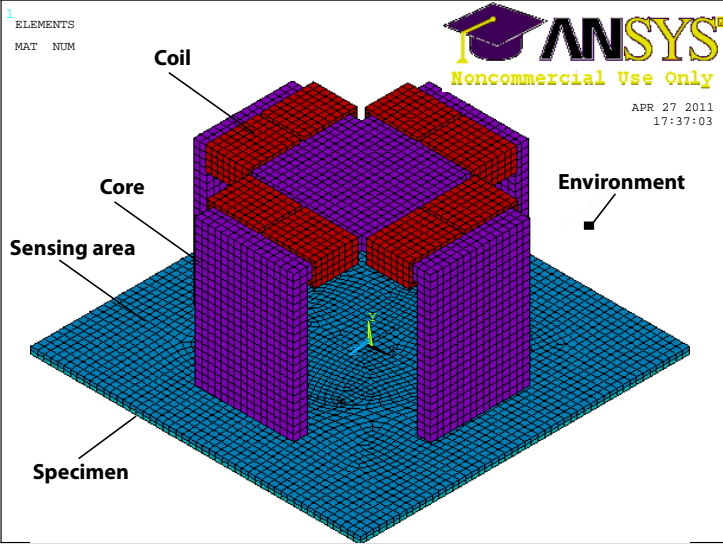
(a)



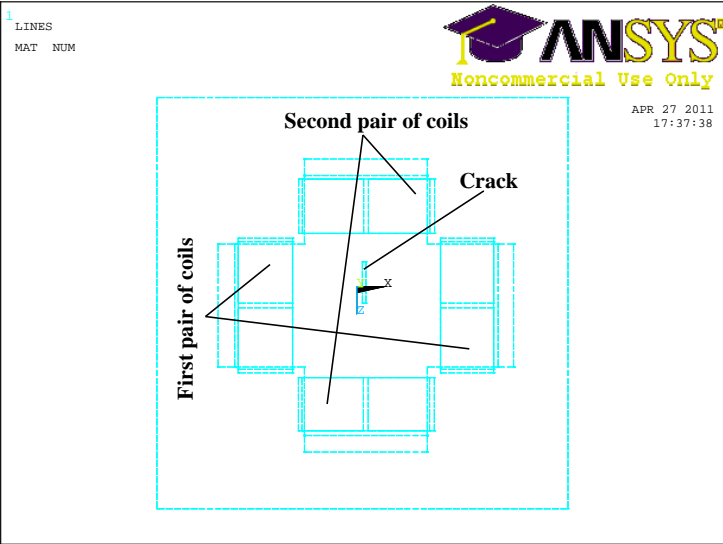
(b)

**Fig. 3-4** Distribution of magnetic density in specimen with vertical crack using yoke type magnetizer. (a) vector solution, (b) nodal solution

*Cross type magnetizer:*



(a)



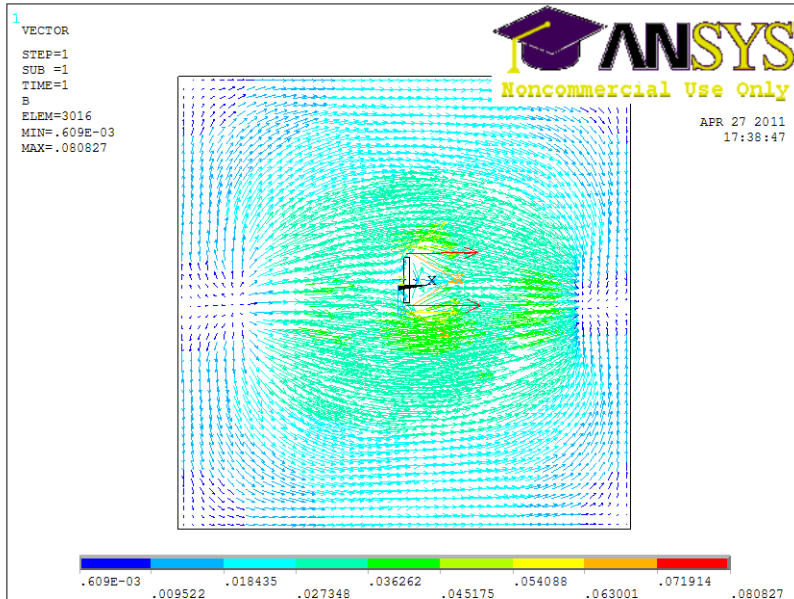
(b)

**Fig. 3-5** Model of system using in ANSYS in the case of cross type magnetizer  
(a) 3-D model, (b) 2-D view

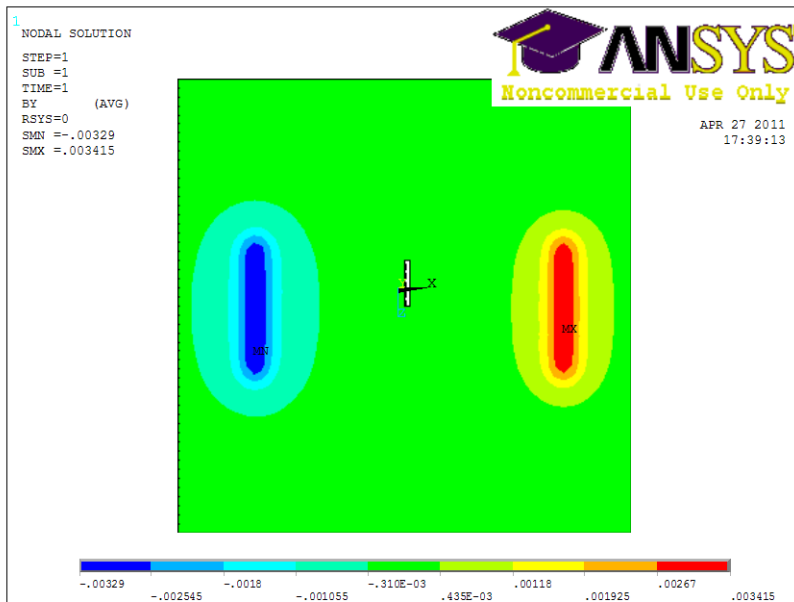
**Table 3-2** Properties of equipments using in ANSYS in the case of cross type magnetizer

<b>Item</b>	<b>Material</b>	<b>Magnetic properties</b>	<b>Size (mm)</b>	<b>Meshing size (mm)</b>	<b>ANSYS model type</b>
Specimen	Steel	MURX 4000 RSVX 8e-6	100 × 100 × 1	2	SOLID117
Core	Mu-metal	MURX 250 RSVX 1.6e-7	72 × 72 × 44	2	SOLID117
Coil	Copper	MURX 1	7 × 33 × 13 4 coils × 100 turns × 0.2A	2	SOLID117
Sensing area	Air	MURX 1	100 × 100 × 1	2	SOLID117
Crack	Air	MURX 1	1 × 10 × 1	2	SOLID117
Environment	Air	MURX 1	120 × 120 × 75	5	SOLID117

Fig. 3-5 shows the model of system using in ANSYS with the cross type magnetizer, and the size, others information in the Table 3-2. The cross type magnetizer has the one core, and the four coils which combined to two pairs of coils. On the specimen, there is the sensing area in which the sensor will be located. All the system was positioned in the air environment which has the shape of rectangular cuboid. Fig. 3-6 and Fig. 3-7 show the simulation results with the vertical crack and horizontal crack, respectively. The current supplied to the first pair of coils to inspect the vertical crack. To inspect the horizontal crack, the currents supplied to the second pair of coils. The magnetic density had the highest value at the two tips of the crack. Thus, the crack could be easily inspected by exchange the current into each pair of coils.



(a)

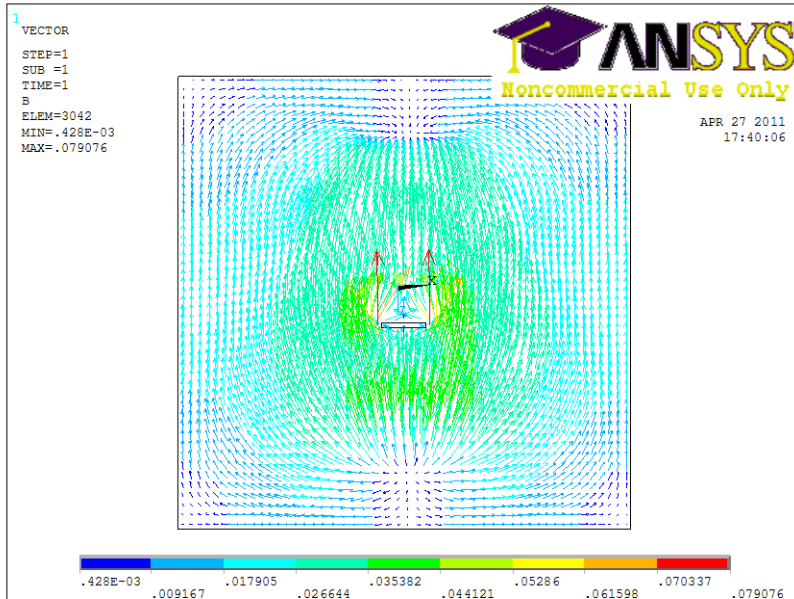


(b)

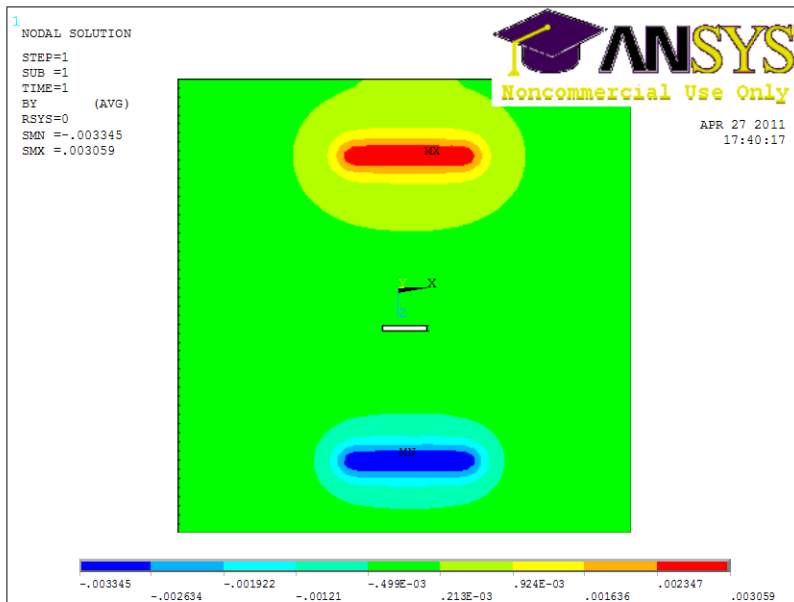
**Fig. 3-6** Distribution of magnetic density on specimen with vertical crack using cross type magnetizer and input current into the first pair of coils.

(a) vector solution, (b) nodal solution





(a)



(b)

**Fig. 3-7** Distribution of magnetic density on specimen with horizontal crack using cross type magnetizer and input current into the second pair of coils.

(a) vector solution, (b) nodal solution

### 3.1.2. Dipole model

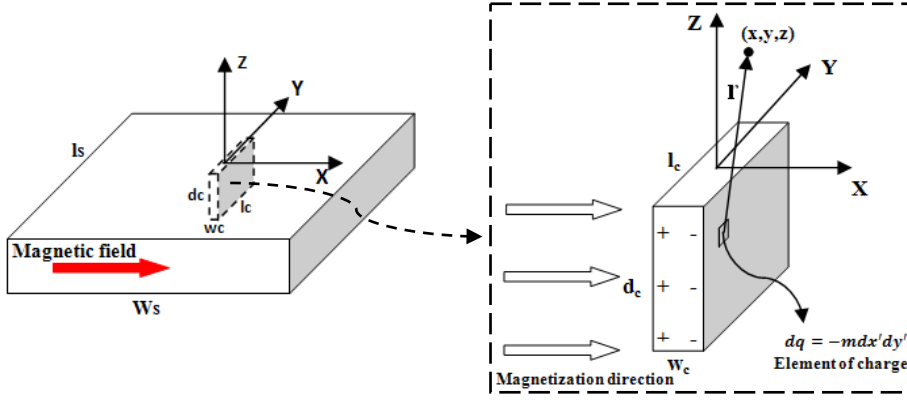


**Fig. 3-8** Dipole model of crack in the case of horizontal magnetization

Fig. 3-8 shows the dipole model and coordinate system for the case of horizontal magnetization. The XY plane is represented on the surface of the specimen, the Y-direction is parallel with the length direction of the crack, the magnetization direction is in the X-direction, and the Z-direction is presented as the vertical direction to the surface of specimen. DMA assumes that magnetic charges exist on both walls of a crack. The magnetic charge of area  $dx'dy'$  is  $dq = -m dx'dy'$ . This magnetic charge induces a magnetic flux density at point  $\mathbf{r}(x, y, z)$  is  $d\vec{H} = \frac{dq}{4\pi\mu r^3} \vec{r}$ . The total magnetic flux density at point  $\mathbf{r}(x, y, z)$  which is induced by magnetic charges on the two walls of crack can be described:

$$\vec{H} = \frac{1}{4\pi\mu} \int_{-\frac{l_c}{2}}^{\frac{l_c}{2}} \int_{-d_c}^0 \frac{m\vec{r}_1}{|\vec{r}_1|^3} dz' dy' - \frac{1}{4\pi\mu} \int_{-\frac{l_c}{2}}^{\frac{l_c}{2}} \int_{-d_c}^0 \frac{m\vec{r}_2}{|\vec{r}_2|^3} dz' dy' \quad (3-1)$$

$$\vec{r}_1 = \left(x + \frac{w_c}{2}, y - y', z - z'\right), \vec{r}_2 = \left(x - \frac{w_c}{2}, y - y', z - z'\right)$$

where,  $m$ ,  $\mu$ ,  $l_c$ ,  $w_c$ ,  $d_c$  and  $z$  are the magnetic charge per unit area, permeability of the specimen, and the length, width, depth of the crack and the lift-off, respectively.

The vertical components of the MFL by Z-direction can be described by the following simple equation [33, 34]:

$$\begin{aligned}
H_z = & \left[ -\ln \frac{(l_c/2 - y) + [(x + w_c/2)^2 + (y - l_c/2)^2 + (z + d_c/2)^2]^{0.5}}{(-l_c/2 - y) + [(x + w_c/2)^2 + (y + l_c/2)^2 + (z + d_c/2)^2]^{0.5}} \right. \\
& + \ln \frac{(l_c/2 - y) + [(x + w_c/2)^2 + (y - l_c/2)^2 + z^2]^{0.5}}{(-l_c/2 - y) + [(x + w_c/2)^2 + (y + l_c/2)^2 + z^2]^{0.5}} \\
& + \ln \frac{(l_c/2 - y) + [(x - w_c/2)^2 + (y - l_c/2)^2 + (z + d_c/2)^2]^{0.5}}{(-l_c/2 - y) + [(x - w_c/2)^2 + (y + l_c/2)^2 + (z + d_c/2)^2]^{0.5}} \\
& \left. - \ln \frac{(l_c/2 - y) + [(x - w_c/2)^2 + (y - l_c/2)^2 + z^2]^{0.5}}{(-l_c/2 - y) + [(x - w_c/2)^2 + (y + l_c/2)^2 + z^2]^{0.5}} \right] \quad (3-2)
\end{aligned}$$

Furthermore, when the crack is moved ( $x_{offset}$ ,  $y_{offset}$ ) and rotated by  $\theta_c$  from its center on the XY plane, the relocated crack position in the new plane  $X_R Y_R$  (Fig. 3-9) can be expressed as the equation (3-3). Thus, the  $H_z$  is changed to  $H_z \cos \theta_c$  [43].

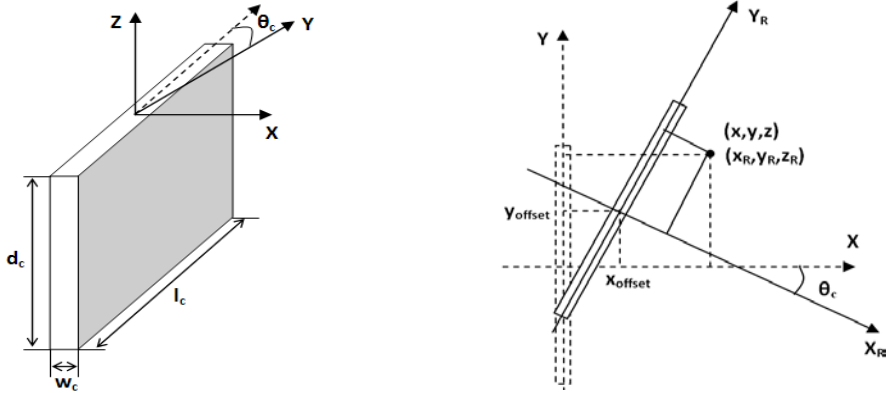


**Fig. 3-9** Relocating position of crack

$$\begin{aligned}
x_R &= (x - x_{offset}) \cos \theta_c - (y - y_{offset}) \sin \theta_c \\
y_R &= (x - x_{offset}) \sin \theta_c + (y - y_{offset}) \cos \theta_c \quad (3-3)
\end{aligned}$$

Equation (3-2) and (3-3) are used with a rectangular crack. To simulate the multiple cracks, we can use the principle of superposition of magnetic field [43]. In which, the total magnetic field at one point is the sum of partial magnetic fields as the equation (3-4).

$$H_{Z,total}(x, y, z) = \sum_{i=0}^n H_{Z,i}(x, y, z) \quad (3-4)$$

With another crack type, we assume it is sum of small rectangular cracks as shown in Fig. 3-10. Thus, the magnetic field can be expressed by equation (3-4). In here, I give some simple crack type such as triangle crack, elliptical crack and step crack. These cracks are divided in to many small rectangular cracks. By this method, the accuracy is depending on the number of divided rectangular crack.

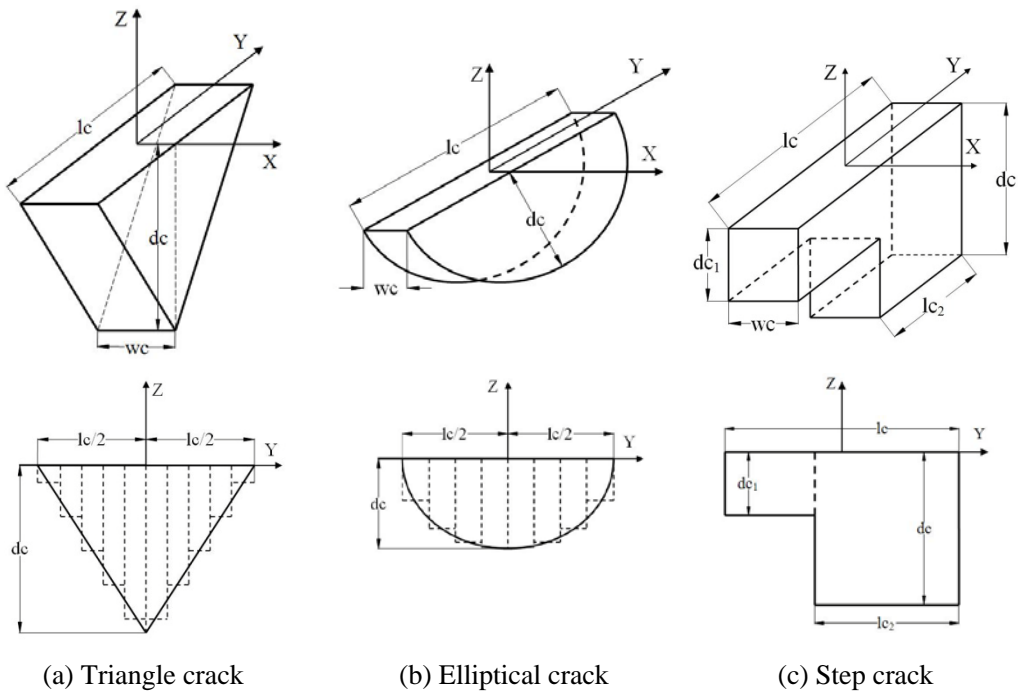


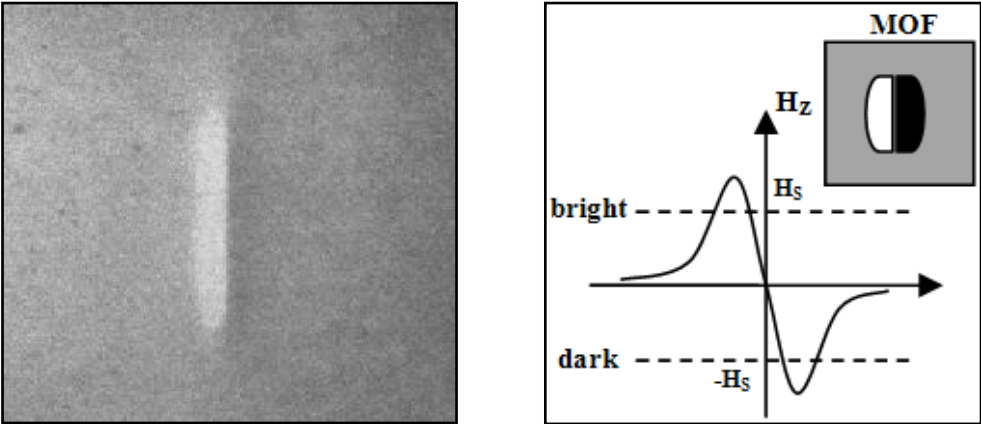
**Fig. 3-10** Different crack shapes and its divided parts

### 3.1.3. Magneto-Optical Image Processing

As the above mention in physical properties of MOF, when the magnetic is higher than positive saturated magnetic field of MOF or smaller than negative saturated magnetic field of MOF, the MOF image is appeared bright or dark area. Depending on the MFL distributes around the crack, the different domains appear on MOF. The magnetic domain around the

crack is larger than in no-crack area. Hence, the bright and dark domains appear large around the crack, the smaller stripe domains appear far from crack as shown in Fig. 3-11(a).

To simulate the MOF image, we used three colors, bright for  $H_z \geq H_s$ , dark for  $H_z \leq -H_s$ , and dusky for  $-H_s < H_z < H_s$  as shown in Fig. 3-11(b) [43]. However, the  $z$  in each equation expresses the lift-off, the distance between the specimen surface and the sensor. The parameters such as magnetic charge per unit  $m$ , permeability of specimen  $\mu$ , saturated magnetic field of MOF  $H_s$ , bias magnetic field,  $H_b$ , and the temperature regime  $T$  were introduced in the software. When bias magnetic field is applied, the total magnetic field distribution is  $H_z + H_b$ . The temperature affects to the value of saturated magnetic field of MOF,  $H_s$  as shown and the spatial resolution of MOF as discussed in chapter two, temperature properties of MOF. The spatial resolution of the MOF was expressed as the meshing number of the 3-D graphic. So, when the temperature  $T$  is changed, the  $H_s$  and meshing number are changed automatically. Thus, we can simplify the principles in the Table 3-3.



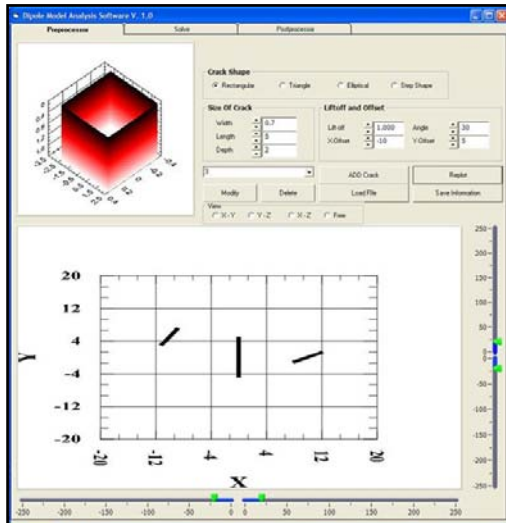
(a) Image of rectangular crack by MOF

(b) Image processing of software

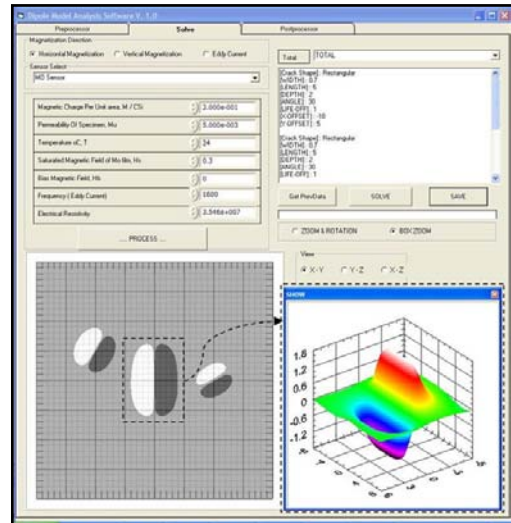
**Fig. 3-11** Image of MOF and image processing of software

**Table 3-3** Relation of real conditions and simulation in the horizontal magnetization

Real conditions	Simulation
Lift-off	Z
Bias magnetic field	$H_{z,total} = H_z + H_{bias}$
Saturated magnetic field of MOF	$H_s$ Bright color for $H_z \geq H_s$ Dark color for $H_z \leq -H_s$ Dusky color for $-H_s < H_z < H_s$
Magnetization direction	Horizontal magnetization
Direction of crack	Angle $\theta_c$
Temperature	Changes the sensitivity of MOF ( $H_s$ ) Changes the width of domain (meshing number of 3-D graphic)



(a) Postprocessor



(b) Simulation

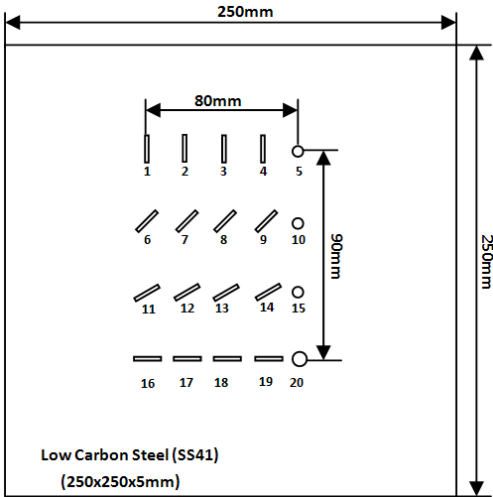
**Fig. 3-12** Software interface

Fig. 3-12 shows the interface of the simulation software. The software was made of Visual Basic 6.0 and 3-D tool (CW3DGraph 6.0 of Measurement Studio by National Instruments Co.). The crack was visualized 3-D that the surface of specimen and depth of the crack were expressed by the XY plane and Z axis of the graphic tool, respectively. The cracks of different types were simulated in the software. Also, a multiple cracks with different direction can be expressed by superposing several graphs, which have the same XY plane and

the same scale of the Z axis as in Fig. 3-12(a). Fig. 3-12(b) shows the parameters and simulation results with different type of magnetizations. The simulation of vertical magnetization and eddy current will be discussed in the next chapters. We can visualize the magnetic distribution in an area by selecting its area.

### 3.1.4. Simulation and experiment results

Fig. 3-13 shows a specimen of 250 x 250 x 5 mm in size which made of low carbon steel (SS41) and multiple cracks which have size in Table 3-4. There are rectangular cracks with different size and angles of  $\theta_c = 0^\circ, 45^\circ, 60^\circ, 90^\circ$ . The cracks No. 5, No. 10, No. 15 and No. 20 are hole types, which were simplified as a square in the numerical analysis. These cracks were machined by using an electro-discharge machine.

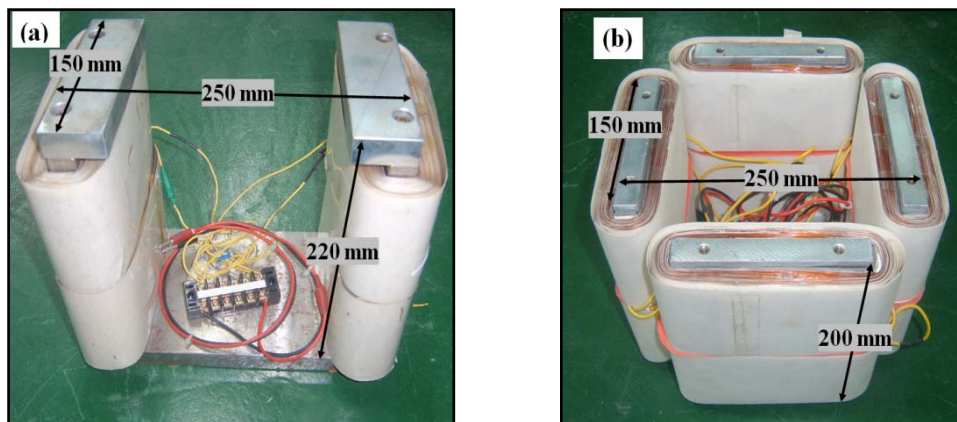


**Fig. 3-13** Cracks on specimen

**Table 3-4** Size of cracks

Number	Width	Depth	Length	Angle	Volume
1	1	0.2	10	0	2
2	1	0.4	10	0	4
3	1	1	10	0	10
4	0.8	0.5	10	0	4
6	1	0.2	10	45	2
7	1	0.4	10	45	4
8	1	1	10	45	10
9	0.8	0.5	10	45	4
11	1	0.2	10	60	2
12	1	0.4	10	60	4
13	1	1	10	60	10
14	0.8	0.5	10	60	4
16	1	0.2	10	90	2
17	1	0.4	10	90	4
18	1	1	10	90	10
19	0.8	0.5	10	90	4
Number	Radius	Depth	Volume		
5	2.5	0.1	1.96		
10	2.5	0.2	3.92		
15	2.5	0.5	9.81		
20	3.5	0.5	19.24		

Fig. 3-14 shows the magnetizers which induce horizontal magnetization in specimen. The Yoke type magnetizer (Fig. 3-14(a)) has 2 cores with 250 mm of the pole distance. Each core is wound by 2000 turns of coil. The cross type magnetizer (Fig. 3-14(b)) has 4 cores which are same with cores of yoke type magnetizer. Each core is also wound by 2000 turns of coil. The cross type magnetizer is similar with a couple of yoke type magnetizer.



(a) Yoke type magnetizer

(b) Cross type magnetizer

**Fig. 3-14** Magnetizers

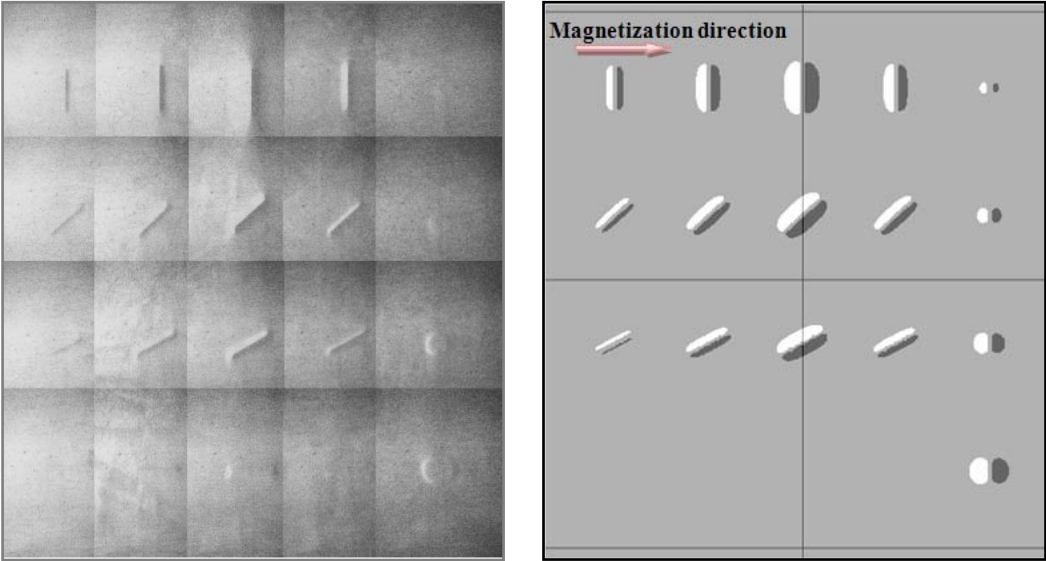
**Table 3-5** Parameters of software using for horizontal magnetization

Lift-off (z )	1 mm
Magnetic charge per unit (m)	0.2
Permeability of specimen ( $\mu$ )	0.005 H/m
Saturated magnetic field of MOF ( $H_s$ )	0.3 mT
Bias magnetic field ( $H_b$ )	0.02 mT
Temperature (T)	24 °C

Fig. 3-15 shows the experiment and simulation result using yoke type magnetizer. The current of 0.1 A is inputted to each coils of yoke type magnetizer in the different direction each other. A magnetic loop is produced and magnetizes the specimen. The simulation parameters are shown in Table 3-5. The experiment results and simulation results were similar in the case of rectangular type cracks. There is bright and dark area around cracks as mention in the principle discussions. The cracks with the angle  $\theta_c = 0^\circ$  (No. 1~No. 4) were easier to detect than the other cases. On the other hand, the cracks with the angle  $\theta_c = 90^\circ$  (No. 16~No. 19) could not be detected. Because the magnetization direction is perpendicular with the length of cracks ( $\theta_c = 0^\circ$ ), and parallel with the length of crack in the case  $\theta_c = 90^\circ$ . In the case of  $\theta_c = 45^\circ$  and  $\theta_c = 60^\circ$ , the cracks were also detected. But the ability of detection reduces depending on the reduction of angle  $\theta_c$ . Also, the ability of detection increased according to the increase of the depth of crack as shown in No. 3, No. 8 and No. 13. However, in the case of hole type cracks, the



simulation results are different with the experiment results because the hole type cracks were assumed as square type cracks in the numerical analysis software. In experiment results, we observe the brightness was lighter in the left hand and darker in the right hand. This is because the north magnetizer pole and south magnetizer pole are on the left and right site of specimen respectively.



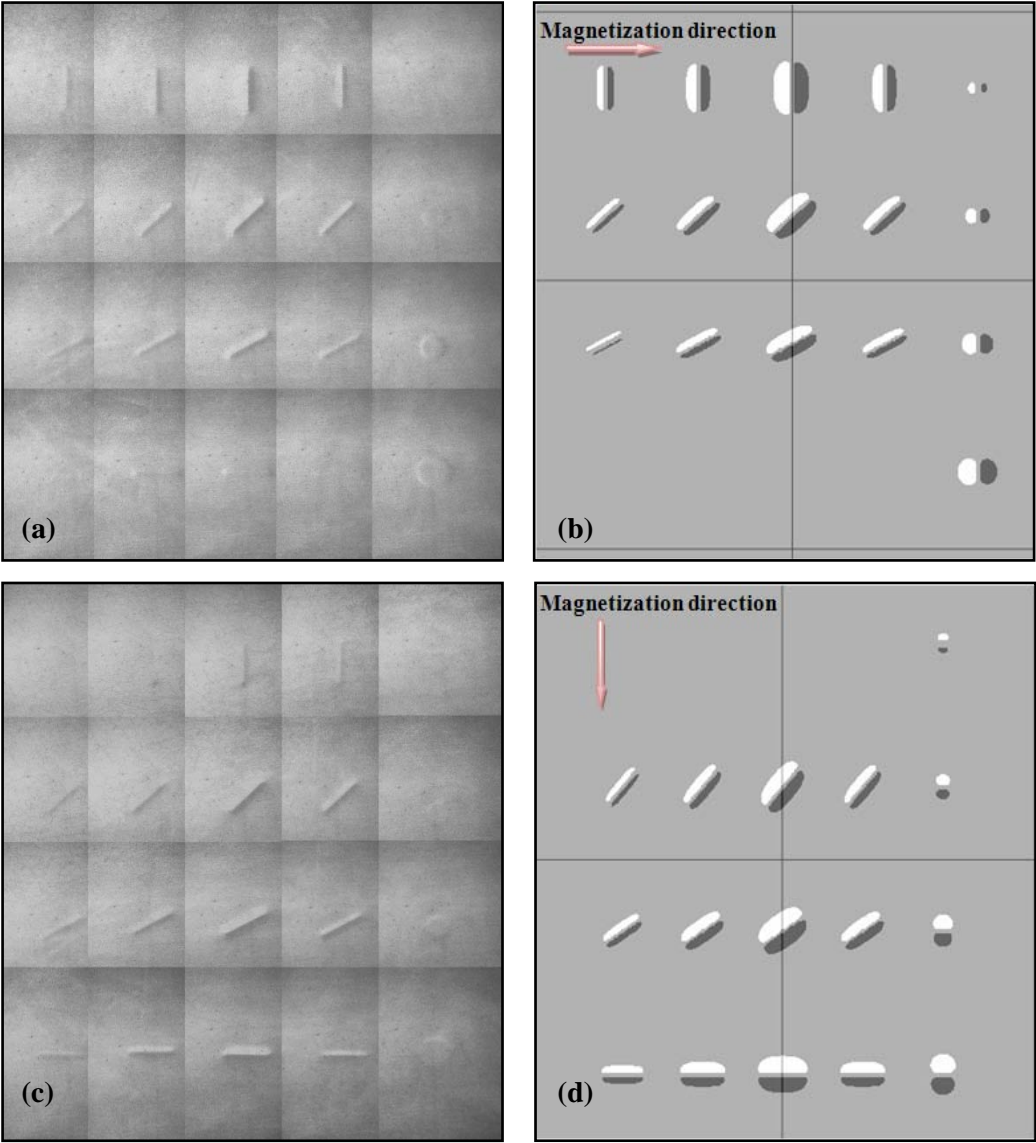
(a) Experiment result

(b) Simulation result

**Fig. 3-15** Experiment and simulation result using Yoke type magnetizer

Fig. 3-16(b),(d) shows the simulation results with the parameters in Table 3-5. Fig. 3-16(a) is experiment results when input a 0.1 A direct current to each pair of coils. When input the current to the pair of coils which is line on the left side and right side of specimen, the horizontal magnetization from left side to right occurs on specimen. Only the cracks of No. 16~19 (Fig. 3-16(a),(b)) did not appear because their length direction are parallel with the magnetization direction. This result is the same with the results of yoke type magnetizer above. By inputting current to another pair of coils which is line on the back side and front side of specimen, we obtain the horizontal magnetization from back side to front side of specimen as shown in Fig. 3-16(d) and experiment results in Fig. 3-16(c). The cracks of No. 1~4 (Fig. 3-16(c),(d)) did not appear because their length direction are parallel with the magnetization

direction. But other cracks were appeared by the same reasons that were discussed in yoke type magnetizer.



Experiment result

Simulation result

**Fig. 3-16** Experiment and simulation result using Cross type magnetizer

However, in cases of No.11~14, these cracks appeared more clearly in Fig. 3-16(c),(d) than in Fig. 3-16(a),(b) because their angle  $\theta_c = 30^\circ$  in Fig. 3-16(a),(b) were changed to the angle  $\theta_c =$

60° in Fig. 3-16(c),(d). Therefore, we can switch the input current between each pair of coils to detect both of  $\theta_c = 0^\circ$  and  $\theta_c = 90^\circ$ . Besides, the information of cracks appeared but not clear at the No. 3, 4 in Fig. 3-16(c) and No. 17, 18 in Fig. 3-16(a) because of the magnetic induction effect between two coil and residual magnetic field in each coils.

### 3.2. Vertical magnetization

#### 3.2.1. Magnetizer and ANSYS simulation

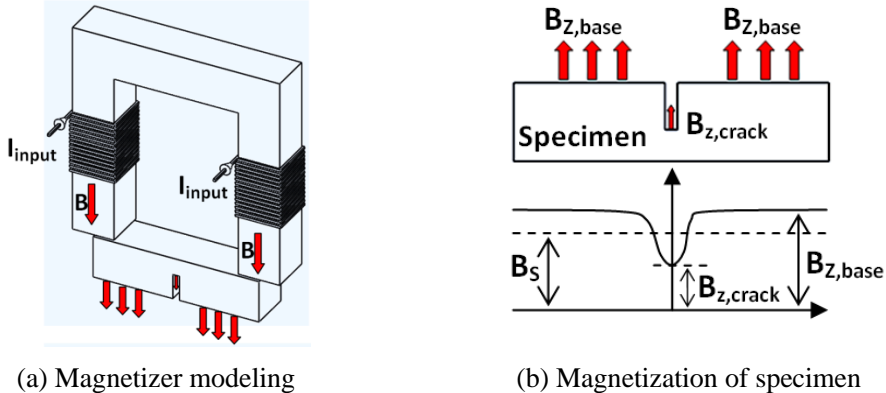
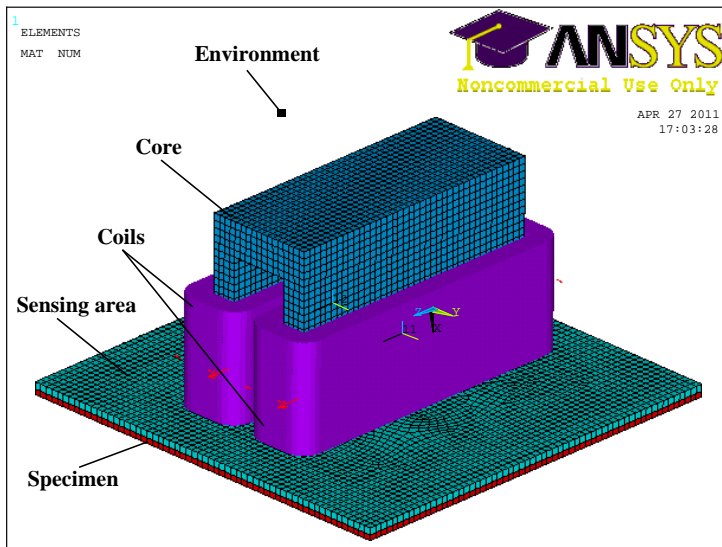


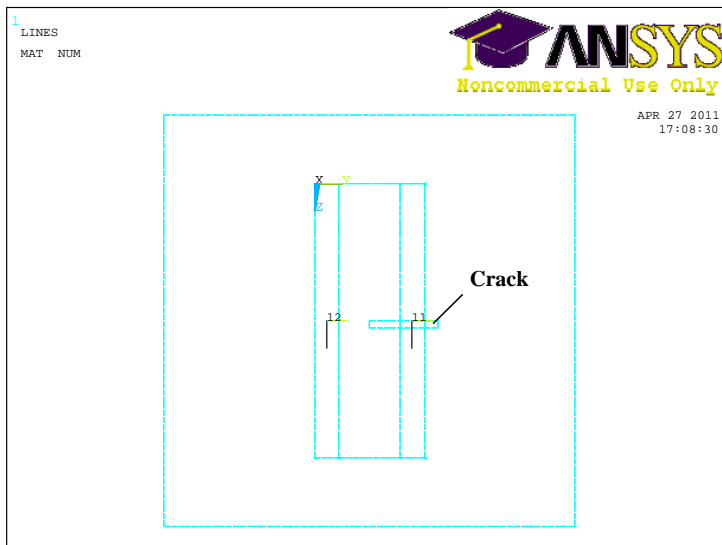
**Fig. 3-17 Model of vertical magnetization**

Vertical magnetic field can be induced by Yoke type magnetizer in which the input currents are in the same direction. When input currents to two coils of Yoke type magnetizer, the magnetic field is induced in the same direction. This magnetic field is vertical with surface of specimen which placed on the cores such as Fig. 3-17(a). The distribution of magnetic field become uniform as the thickness of specimen increased. If the specimen has a crack, the distribution of magnetic field will be different. The magnetic field at lift-off,  $z_{liff}$  is  $B_{z,base}$ , which is almost uniform in the no-crack areas. However, the lift-off is  $z_{liff} + d_c$  ( $d_c$  is the depth of crack) on top of crack. Thus, the magnetic field  $B_{z,crack}$  will be lower as shown in Fig. 3-17(b).

For more detail about this kind of magnetizer, we analyzed the performance of it by FEM using ANSYS program (Ver. 11.0 SP1 UP20070830, EMAG).



(a)



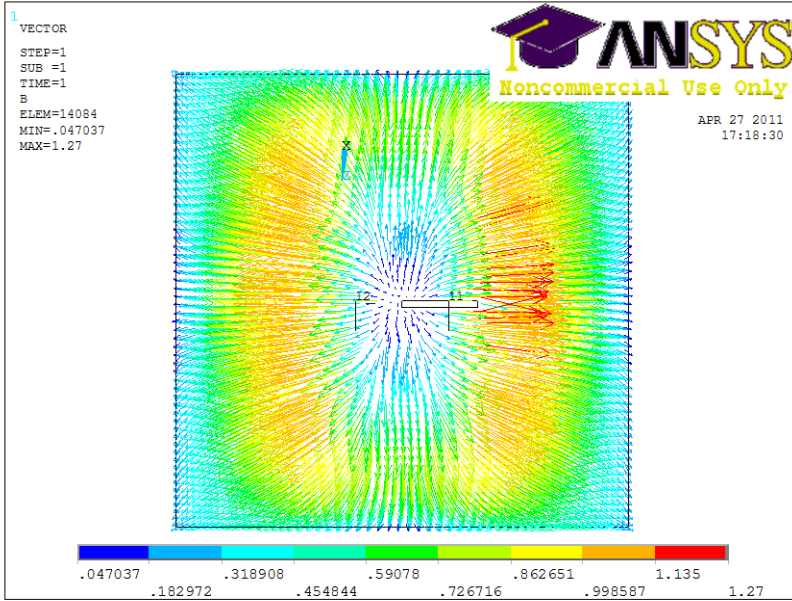
(b)

**Fig. 3-18** Model of system using in ANSYS in the case of vertical magnetizer  
(a) 3-D model, (b) 2-D view

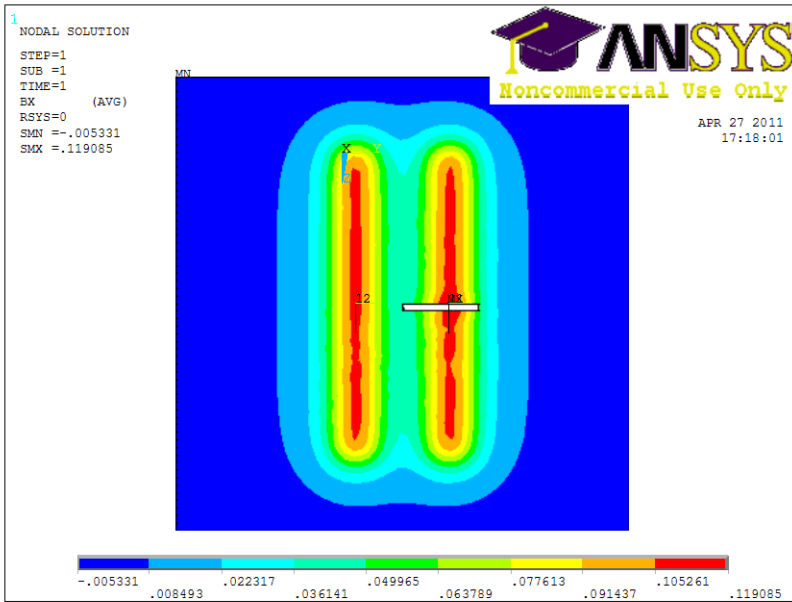
**Table 3-6** Properties of equipments using in ANSYS in the case of vertical magnetizer

<b>Item</b>	<b>Material</b>	<b>Properties</b>	<b>Size (mm)</b>	<b>Meshing size (mm)</b>	<b>ANSYS model type</b>
Specimen	Steel	MURX 4000 RSVX 8e-6	60 × 60 × 0.8	1	SOLID117
Core	Mu-metal	MURX 250 RSVX 1.6e-7	16 × 40 × 27	1	SOLID117
Coil	Copper	MURX 1	9.7 × 47 × 16 2 coils × 200 turns × 4.08 A	1	SOURCE36
Sensing area	Air	MURX 1	60 × 60 × 1	1	SOLID117
Crack	Air	MURX 1	1 × 10 × 1	1	SOLID117
Environment	Air	MURX 1	74 × 80 × 42	5	SOLID117

Fig. 3-18 shows the model of system using in ANSYS with the vertical magnetizer with the size and others information in the Table 3-6. The vertical magnetizer is the yoke type magnetizer, which has the one core and the two coils which was applied the currents with the different direction each other. On the specimen, there is the sensing area in which the sensor will be located in. All the system was located in the air environment which has the shape of rectangular cuboid. Fig. 3-19 and Fig. 3-20 show the simulation results with the horizontal crack and vertical crack, respectively. In the both of two cases, the magnetic field was almost not effected by the direction of crack.

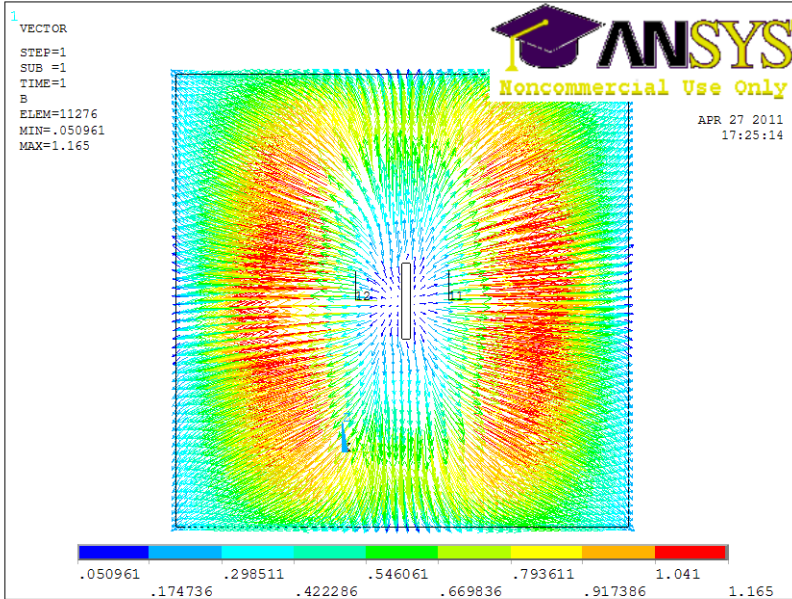


(a)

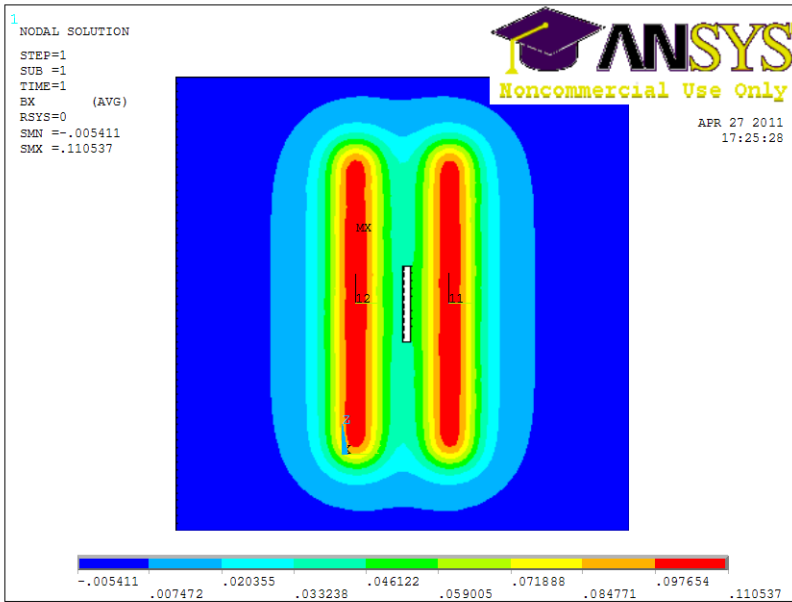


(b)

**Fig. 3-19** Distribution of magnetic density in specimen with horizontal crack using vertical magnetizer. (a) vector solution, (b) nodal solution



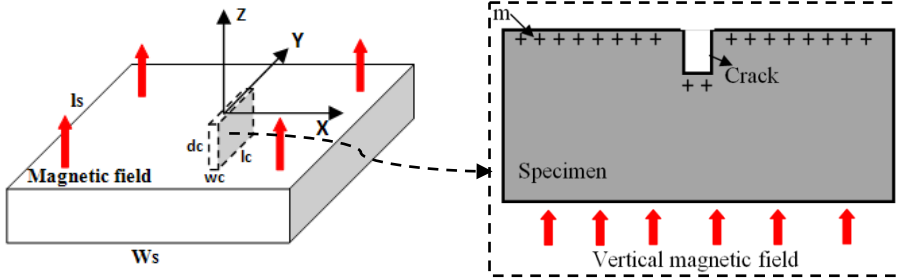
(a)



(b)

**Fig. 3-20** Distribution of magnetic density in specimen with vertical crack using vertical magnetizer. (a) vector solution, (b) nodal solution

### 3.2.2. Dipole model



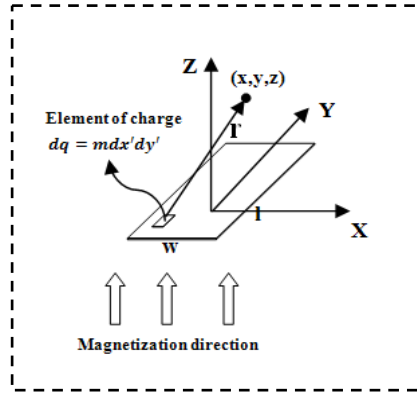
**Fig. 3-21** Dipole model of crack in the case of vertical magnetization

Fig. 3-21 shows the dipole model of crack in the case of vertical magnetization. The magnetic charge ( $m$ ) is assumed to be uniform occurs on the surface of specimen and at the bottom of crack. We can consider that  $m$  is distributed on the whole surface of specimen by width  $w_s$  and length  $l_s$  (the magnetic flux intensity would be  $H_{Z,all}$ ). And at the bottom of crack by width  $w_c$  and length  $l_c$  at the distance in the  $Z$ -direction (the magnetic flux intensity would be  $H_{Z,crack}$ ). At the bottom of this crack,  $m$  is distributed with width  $w_c$ , length  $l_c$  and at the  $d_c$  distance in the  $Z$ -direction (the magnetic flux intensity would be  $H_{Z,under}$ ). Fig. 3-22 shows the method to calculate the magnetic field of an area magnetic charge. Similar with the method used in the case of horizontal magnetic field, we use the integration method. With an area ( $w \times l$ ) magnetic charge, the magnetic flux density at point  $\mathbf{r}(x, y, z)$  by  $Z$ -direction can be expressed by equation (3-5) [30, 33]. The distribution of magnetic field of the overall can be calculated by the equation (3-6). The relocated position of crack is described by equation (3-3). The value of magnetic field is not effected by direction of the length of crack.

$$H_z = \frac{m}{4\pi\mu} \int_{-\frac{l}{2}}^{\frac{l}{2}} \int_{-\frac{w}{2}}^{\frac{w}{2}} \frac{z}{\{(x-x')^2 + (y-y')^2 + z^2\}^{3/2}} dx' dy' \quad (3-5)$$

$$H_{Z,total} = H_{Z,all} - H_{Z,crack} + H_{Z,under} \quad (3-6)$$





**Fig. 3-22** Calculation of magnetic field by an area magnetic charge

### 3.2.3. Magneto-Optical Image Processing

**Table 3- 7** Relation of real conditions and simulation in the vertical magnetization

Real conditions	Simulation
Lift-off	$z$
Bias magnetic field	$H_{z,total} = H_z + H_{bias}$
Saturated magnetic field of MOF	$H_z$ Bright color for $H_z > H_s$ Dusky color for $H_z < H_s$
Magnetization direction	Horizontal magnetization
Temperature	Changes the sensitivity of MOF ( $H_s$ ) Changes the width of domain (meshing number of 3-D graphic)

As mentioned above, the magnetic field domain on specimen has two domains. One is almost uniform in the no-crack areas,  $H_{z,base}$ . One is lower value,  $H_{z,crack}$ . These two magnetic field values can be controlled by controlling the input currents to coils of magnetizer. In the MOI experiment, the  $H_{z,base}$  is controlled to be slightly larger than saturated magnetic intensity of MOF,  $H_s$ , and the  $H_{z,crack}$  will be lower value than  $H_s$ . Thus, the crack would occur on MOF as shown in Fig. 3-23. The software has two colors, bright color for  $H_z > H_s$  and dusky color for  $H_z < H_s$ . The algorithm is simplified as shown in the Table 3- 7.

Fig. 3-24 shows an example of the cracks with different size and direction. The vertical crack on the left side has the size of width 2 mm, length 10 mm, and depth 2 mm. And the rotated crack on the right side has the size of width 3 mm, length 10 mm, depth 2 mm, and rotated angle  $45^{\circ}$ . The direction of crack doesn't affect to the inspection ability of MOF.

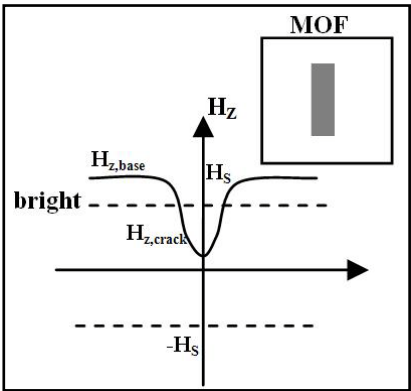


**Fig. 3-23** MOF processing

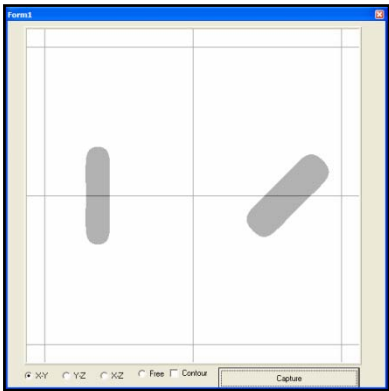


**Fig. 3-24** MOF of Multiple cracks

*3.2.4. Simulation and experiment results*

Fig. 3-25 shows the simulation result (a) and experimental result (b) in the case of vertical magnetization. A rectangular crack with 0.5mm of width, 10mm of length and 4mm of depth on SS41 specimen was used. The yoke type magnetizer (Fig. 3-14(a)) was used to induce vertical magnetization by input the 0.17 A direct current to two coils in the same direction. The parameters for simulation are shown in Table 3-8. In the both results, only the information of crack was appeared. In the case of simulation result (Fig. 3-25(a)), the information of crack appeared with dusky color, and the no-area crack appeared with bright color as mention in principle discussions. Because the magnetic field in crack area  $H_{z,crack}$  ,  $-H_s < H_{z,crack} < H_s$  and the magnetic field in no-crack area  $H_{z,no crack}$  ,  $H_{z,no crack} > H_s$ . In the experiment result (Fig. 3-25(b)), the crack appeared with dark color but not smoothly cause of noises.

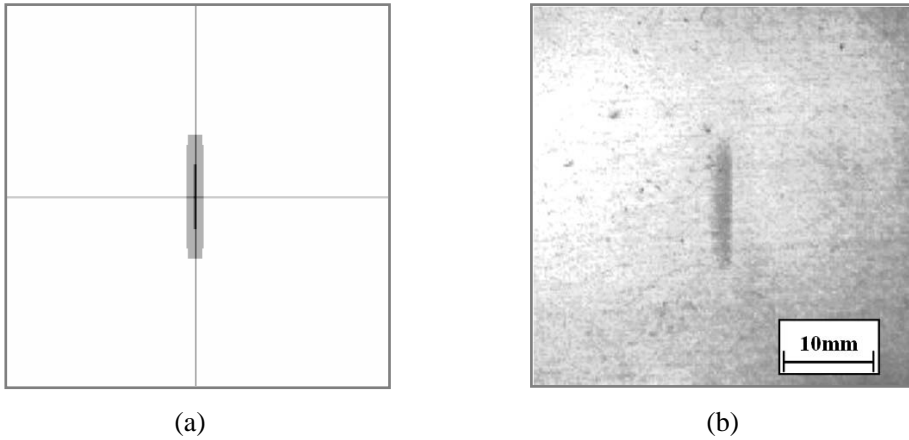


**Fig. 3-25** Simulation results (a) and experiment results (b)

**Table 3-8** Parameters of software using for vertical magnetization

Lift-off ( $z$ )	1 mm
Magnetic charge per unit ( $m$ )	0.0028
Permeability of specimen ( $\mu$ )	0.005 H/m
Saturated magnetic field of MOF ( $H_s$ )	0.3 mT
Bias magnetic field ( $H_b$ )	0.05 mT
Temperature (T)	24 $^{\circ}$ C

# Chapter 4

## ALTERNATIVE MAGNETIC FIELD

### 4.1. Model of MOI system and ANSYS simulation of STIC

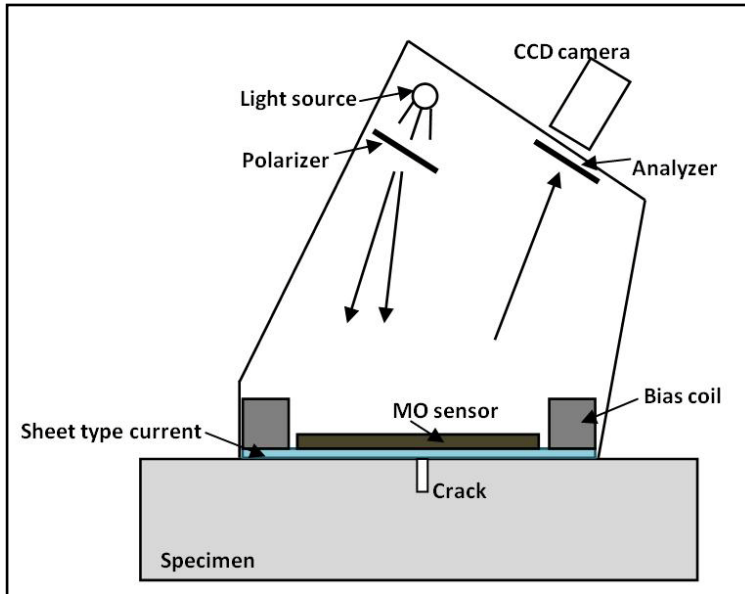


**Fig. 4-1** Model of MOI system

Fig. 4-1 shows the model of MOI system [38, 44] which is placed on a specimen. It has a sheet type foil which contains an induced sheet type current. This induced sheet type current can be induced by an alternative magnetic field, and induces an induced Eddy current in the specimen. The induced Eddy current will be distorted because of presence of cracks. An alternative magnetic field will be induced normally to the surface of a MO sensor. The MOI system has a polarizer to polarize a light beam when pass through it. An analyzer receives the reflected polarized light from a MO sensor. This analyzer usually forms with the polarizer a fixed angle. Because of the Faraday effect, the plane of polarized light is rotated by different angles after reflecting from MO sensor. Thus, a CCD camera will form an MOI by black and white colors, according to the Faraday angles. In here, we will discuss how to simulate this alternative magnetic field.

This MOI system is usually used in inspection of crack on paramagnetic material such as aluminum, stainless steel, and widely used in the aerospace industry. Fig. 4-2 shows two examples of MOI using alternative magnetic field (by U.S. Department of Transportation, Federal Aviation Administration) [45]. The system can inspect fatigue cracks, corrosions, etc.

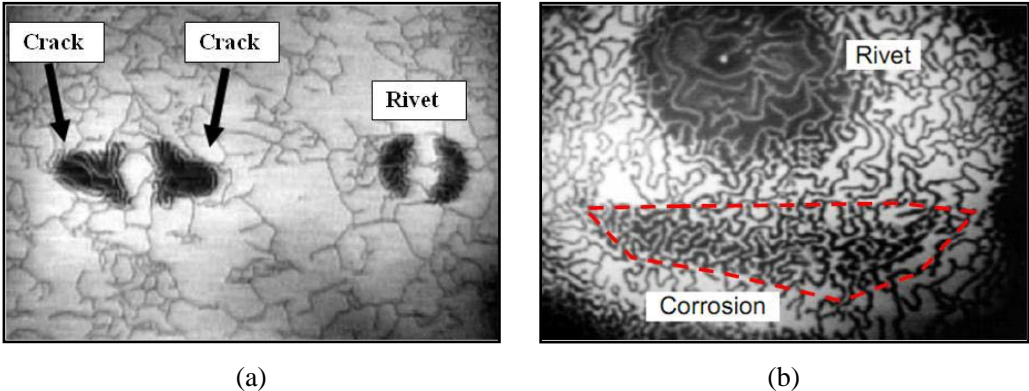


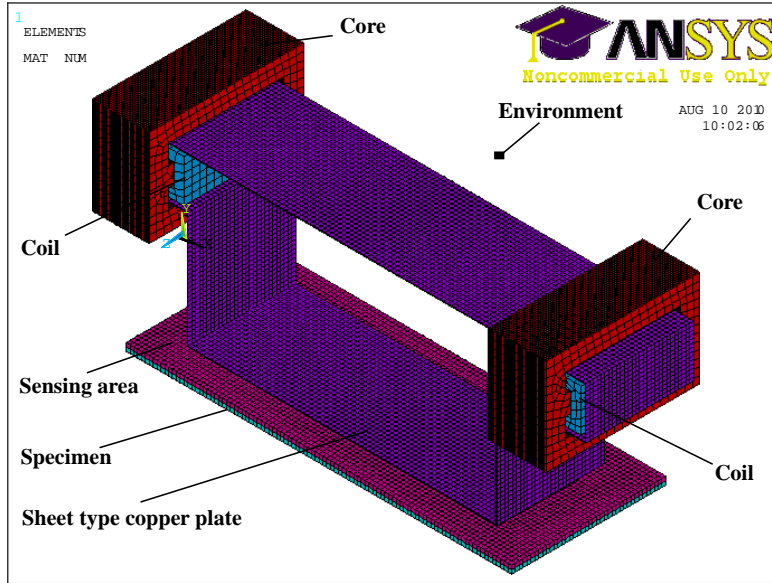
**Fig. 4-2** Images of MOI.

(a) Single Eddy current direction, (b) Multiple Eddy current direction

*Obtained by U.S. Department of Transportation, Federal Aviation Administration*

Fig. 4-3 shows the model of STIC in ANSYS program (Ver. 11.0 SP1 UP20070830, EMAG). The model has the two cores which combined of 30 small slide cores in each. The two coils turned around these cores and were supplied by alternative current (AC). An alternative magnetic field was appeared around the two cores and induced sheet type current on sheet type copper plate. The sensing area and specimen were place under the sheet type copper plate. Thus, the eddy current appeared around a crack in the specimen. All the components were place inside the rectangular cuboid of air (environment). The components have the properties using in ANSYS program, were shown in the Table 4-1.

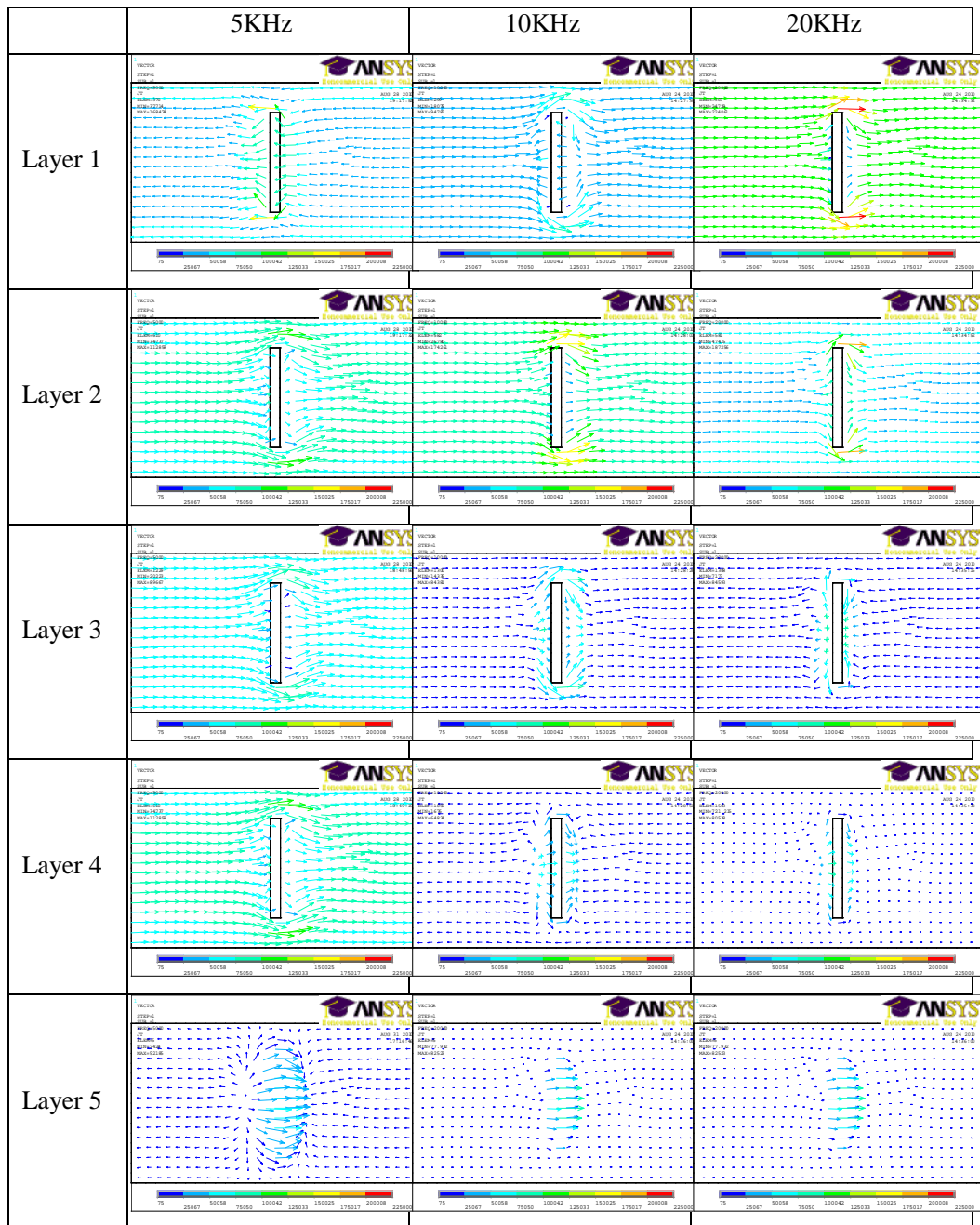
Fig. 4-4 shows the Eddy current flows of each layer of the specimen, the simulation results using ANSYS program. The frequency of 5 KHz, 10 KHz, 20 KHz, and current of 2.5 A were supplied into the coils. Because of skin effect, the Eddy current decreased according to the increasing of layer number (the increasing of the depth from the surface of specimen) because of skin effect; and the higher frequency had the higher Eddy current at the near surface of specimen.

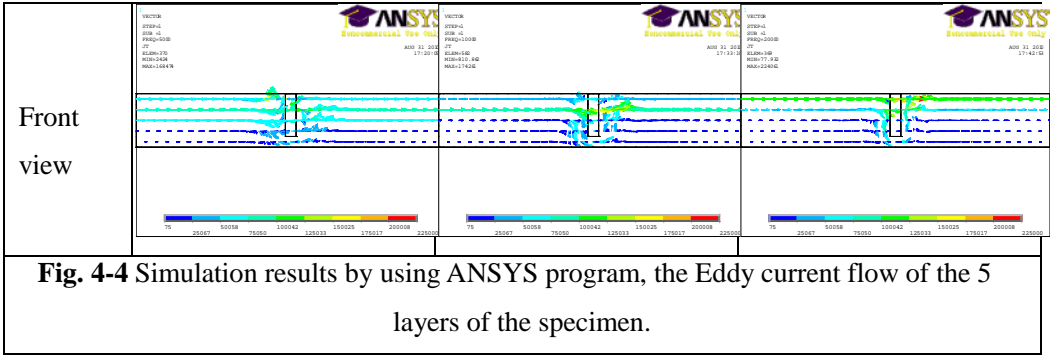


**Fig. 4-3** Model of system using in ANSYS in the case of STIC

**Table 4-1** Properties of equipments of STIC using in ANSYS

Item	Material	Magnetic Properties	Size (mm)	Meshing size (mm)	ANSYS model type
Specimen	Aluminum	MURX1.000022 RSVX 2.82e-8	40 × 100 × 1	1	SOLID117
Core	Silicon Steel	MURX 4000 RSVX 4.72e-8	25 × 40 × 0.35 2 cores with 30 slides of each.	2	SOLID117
Coil	Copper	MURX0.999994 RSVX 1.68e-8	21 × 28 × 11 2 coils × 17 turns × 2.5A	2	SOLID117
Sheet type copper plate	Copper	MURX0.999994 RSVX 1.68e-8	28 × 126.4 × 44 thickness 0.2	1	SOLID117
Sensing area	Air	MURX 1	40 × 100 × 1	1	SOLID117
Crack	Air	MURX 1	1 × 10 × 4	2	SOLID117
Environment	Air	MURX 1	50 × 170 × 70	5	SOLID117





## 4.2. The first suggestion

### 4.2.1. Dipole model

As in the previous study (3.1), when a static magnetic field is applied to a specimen, the crack is assumed to be filled by dipoles with dipole moments oriented opposite to the direction of the applied magnetic field (Fig. 4-5(a)). These magnetic dipoles are the function of shape and size of crack as describe in the equation (4-1).

$$m_{MFL} = m_{MFL}(shape, w_c, l_c, d_c) \tag{4-1}$$

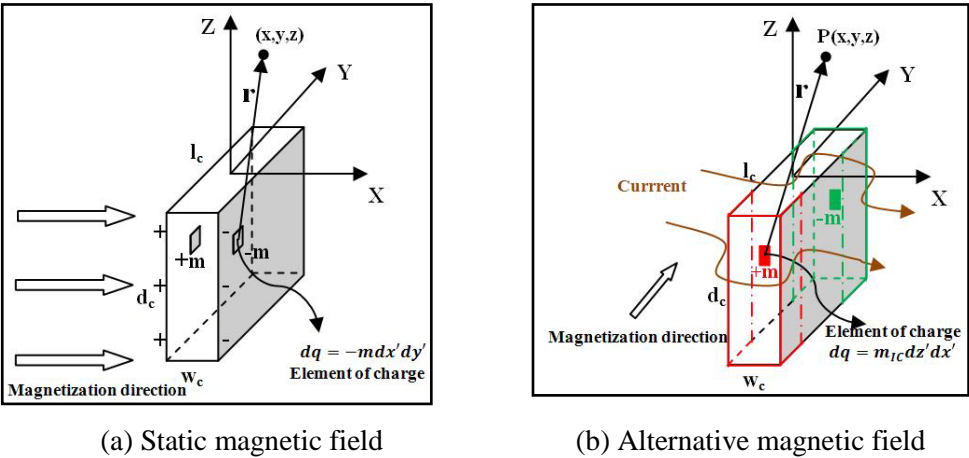


Fig. 4-5 Dipole model



When an alternative magnetic field, which is parallel with the length of crack, is applied to a paramagnetic material specimen, an eddy current will appear perpendicular to the length of the crack on the specimen. Because of the crack, this eddy current distorts greatly around both tips of the crack, as shown in Fig. 4-6. The eddy current changes with depth from the surface of the specimen by the skin effect, which is described by equation (4-2).

$$\frac{J_t}{J_s} = e^{-\frac{t}{\delta}} \quad (4-2)$$

$$\delta = \frac{1}{\sqrt{\pi f \mu \sigma}}$$

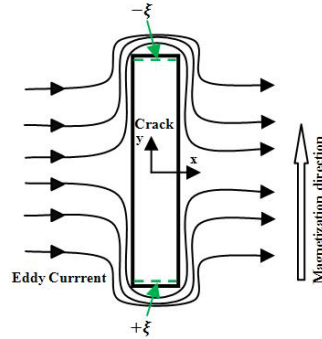


**Fig. 4-6** Eddy current flow – the first suggestion

where  $t, f, \mu, \sigma, J_t, J_s$  are respectively the depth from the surface, frequency of the alternative magnetic field, absolute permeability of the specimen, electrical conductivity, current density at depth  $t$  and current density at the surface of the specimen.

Thus, we assume that dipole magnetic charges appear at both tips of the crack, as shown in Fig. 4-6. Therefore, the distribution of an alternative magnetic field around crack can be described by equation (4-3) in the first half cycle of frequency and by the inverse sign in the second half cycle:

$$\vec{H}_{IC} = \frac{1}{4\pi\mu} \int_{-\frac{w_c}{2}}^{\frac{w_c}{2}} \int_{-d_c}^0 \frac{m_{IC} \vec{r}_3}{|\vec{r}_3|^3} dz' dx' - \frac{1}{4\pi\mu} \int_{-\frac{w_c}{2}}^{\frac{w_c}{2}} \int_{-d_c}^0 \frac{m_{IC} \vec{r}_4}{|\vec{r}_4|^3} dz' dx' \quad (4-3)$$

$$\vec{r}_3 = \left( x - x', y + \frac{l_c}{2}, z - z' \right), \vec{r}_4 = \left( x - x', y - \frac{l_c}{2}, z - z' \right)$$

$$m_{IC} = m_{IC}(f, t, shape, w_c, l_c, d_c)$$

$m_{IC}$  is a function of the  $f, t$ , shape, and size of crack. We assume that:

$$m_{IC} = \xi e^{-\frac{t}{\delta}} \quad (4-4)$$

where  $\xi = \xi(\text{shape}, w_c, l_c, d_c)$  is the magnetic charge factor. Thus,  $m_{IC}$  is similar with the  $m_{MFL}$  in equation (4-1).

Then, the magnetic field distribution around a crack in the  $z$  direction can be described by the simple equation (4-5) in the first cycle of frequency and by the inverse sign in the second cycle:

$$H_z = \frac{\xi}{4\pi\mu} \int_{-w_c/2}^{w_c/2} \int_{-d_c}^0 \frac{e^{\frac{z'}{\delta}}(z-z')}{\{(x-x')^2 + (y+lc/2)^2 + (z-z')^2\}^{3/2}} dz' dx' \quad (4-5)$$

$$- \frac{\xi}{4\pi\mu} \int_{-w_c/2}^{w_c/2} \int_{-d_c}^0 \frac{e^{\frac{z'}{\delta}}(z-z')}{\{(x-x')^2 + (y-lc/2)^2 + (z-z')^2\}^{3/2}} dz' dx'$$

#### 4.2.2. Magneto-optical image processing

Fig. 4-7 shows the schematic of the Magneto-Optical System, which combines the sheet current excitation (eddy current) with the MOF effect [38, 44]. In this figure, currents in the first half of the cycle are indicated by solid lines, and currents in the second half of the cycle are indicated by dotted lines. The eddy current is distorted by the cracks, and it produces a magnetic field normal to the surface of MOF. In addition, the bias magnetic field, which is normal to the surface of MOF, is applied to the MO sensor. The resultant total magnetic field is applied to the MOF, and a magneto-optical image (MOI) is induced. All these magnetic domains at the crack area are smaller value than the minus saturated magnetic field of the MOF, and these domains appear as dark areas on the MOI. While the areas far from the crack have higher values, they will appear as smaller dark stripe lines on the MOI.

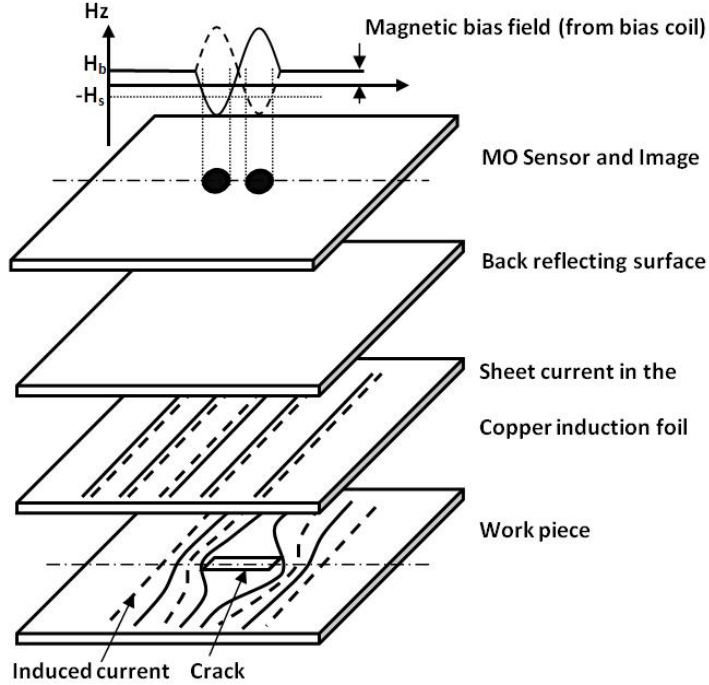


**Fig. 4-7** Schematic of MOI System

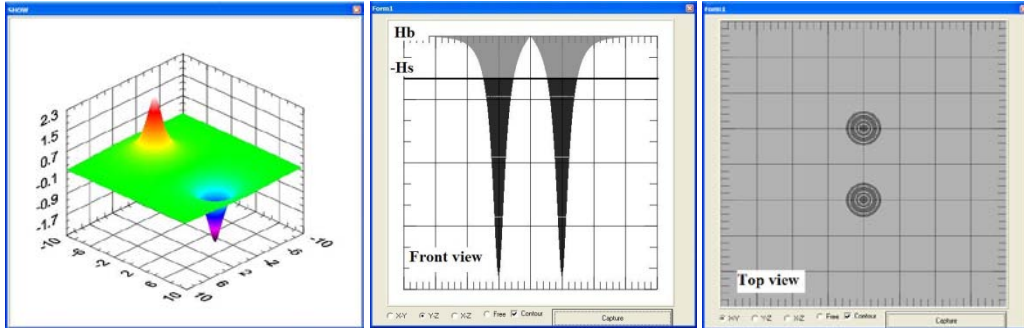
To simulate the MOI, an image processing algorithm is used.  $H_{z1}$ ,  $H_{z2}$ ,  $H_b$ ,  $H_s$  are the first half cycle, second half cycle, bias magnetic field and saturated magnetic field of the MOF.  $H_{z1}$  and  $H_{z2}$  are obtained from equation (4-5), with  $H_{z2} = -H_{z1}$ . The total magnetic field can be described by equation (4-6):

$$H_z = -abs(H_{z1}) + H_b \quad (4-6)$$

The MOI has two colors, a dark area if  $H_z \leq -H_s$  and a dusky color if  $H_z > -H_s$ . In addition, the temperature affects the value of  $H_s$  and the spatial resolution of the MOF. These properties of MOF can be expressed in the software by changing the value of  $H_s$  according to the temperature, and the spatial resolution is expressed by the meshing number of the 3D plots. So, when temperature changes, the  $H_s$  and meshing number are changed automatically. The algorithm is simplified as shown in the Table 4-2.

**Table 4-2** Relation between real condition and simulation

Real Condition	Simulation
Properties of material	Absolute permeability ( $\mu$ ) Electrical conductivity ( $\sigma$ )
Lift-off	$z$
Frequency	$f$
Bias magnetic field and alternative magnetic field	$H_z = - H_{z1}  + H_b$
Saturated magnetic field	$H_s$ Dark color for $H_z \leq -H_s$ Dusky color for $H_z > -H_s$
Temperature	Changing the sensitivity of MOF ( $H_s$ ) Changing the spatial resolution of MOF (meshing number of 3D graphic)



(a) First half cycle

(b) After MOI processing

**Fig. 4-8** Magnetic distribution and Image processing

Fig. 4-8 shows the plot of the magnetic distribution which is induced by eddy current. The magnetic field in the first half cycle is shown in Fig. 4-8(a). The magnetic field is maximum and minimum at the tips of the crack and reversed in the second half cycle. Fig. 4-8(b) shows the magnetic processing and the MOI processing which is described by equation (4-6). The magnetic domain is dark color if its value is less than the minus saturated magnetic

field ( $-H_s$ ), while dusky color if its value is higher than  $-H_s$ . For easy viewing of the magnetic domain with different  $H_s$ , we plot some contour lines, as shown in the top view picture (Fig. 4-8(b)).

4.2.3. Magneto-optical image processing

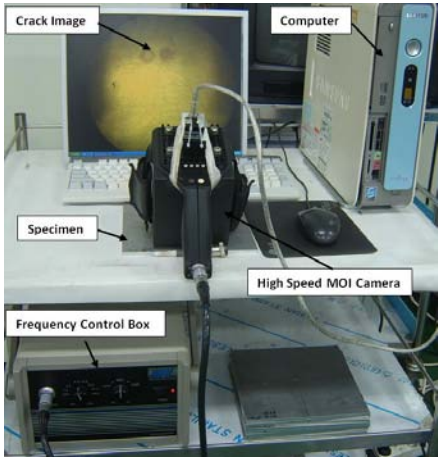


Fig. 4-9 Experiment setup

Table 4-3 Size of cracks

Number	Width (mm)	Length (mm)	Depth (mm)
1	0.7	10	1
2	0.7	10	2
3	0.7	10	3

Table 4-4 Simulation parameters

Lift-Off ( $z$ )	1 mm
Magnetic charge factor ( $\xi$ )	1e-4
Permeability of Specimen ( $\mu$ )	1.2566e-6 H/m
Electrical conductivity ( $\sigma$ )	3.5461e+7 S/m
Saturated magnetic field of MOF ( $H_s$ )	0.3 mT
Bias magnetic field ( $H_b$ )	0.05 mT
Temperature (T)	24 °C

The specimens of 250 x 250 x 5 mm size were made of aluminum alloy (A17075). Each specimen had a rectangular crack (Table 4-3) at the center, which was machined by using an electric discharge machine. Fig. 4-9 shows the experiment setup, and the MOI taken by a the high speed MOI camera, which was made by PRI Co. MOI, has two buttons to control the bias magnetic field and a case box to control the frequency from 1.6 KHz to 102.4 KHz.

Fig. 4- 10 shows the experiment and simulation results for cracks of different sizes and frequencies in Table 4-3. Table 4-4 shows the simulation parameters. Each photograph of the experiment results (Fig. 4- 10 (a)) show two groups of black triples, which are the magnetic domains of the crack tips. The size of each group increases with crack depth. Because of the skin effect, this size decreases due to the increase of frequency. Each group is similar with cam shape which is taper at one side. At crack No.1, which has the smallest crack depth, this size show little change because of low skin effect. Fig. 4- 10(b) shows the simulation results. Each

photograph has two black areas at the tips of the crack. And, their sizes increase with increase of crack depth and decrease of frequency. Thus, the simulation results were similar with the experiment results. But, these areas are circular, which is different from the experiment results. Consequently, we need to improve our method.

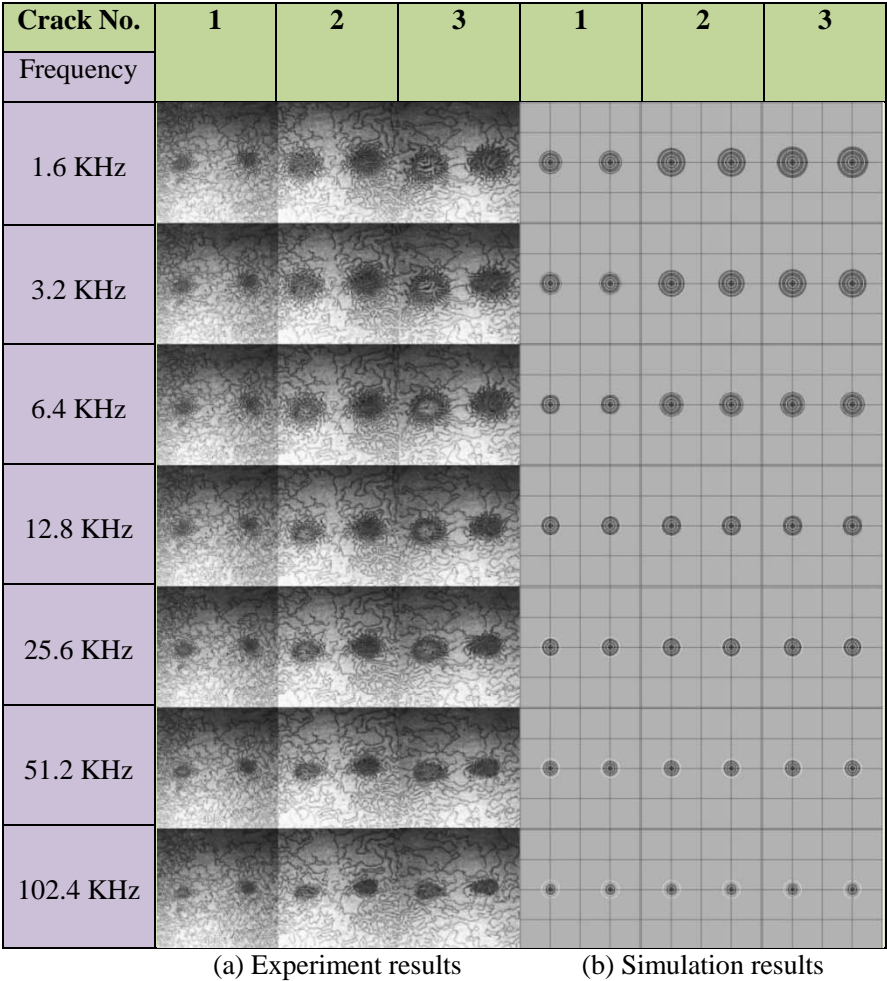


**Fig. 4- 10** Results with the second suggestion

### 4.3. The second suggestion

#### 4.3.1. Dipole model

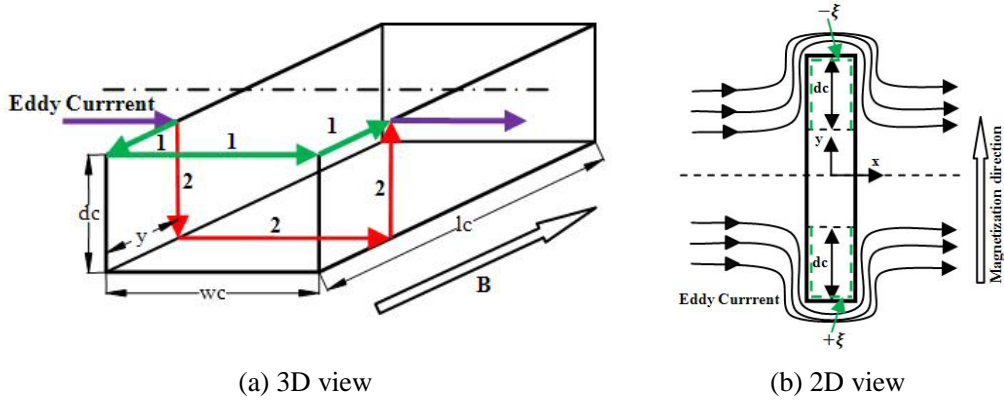


**Fig. 4-11** Eddy current flow of one half cycle- the second suggestion

Fig. 4-11 shows the eddy current flow for a crack. When the eddy current approaches a crack, it has two ways to pass through the crack, as shown in Fig. 4-11(a), but it has to choose the shortest way. In Fig. 4-11(a), way “1” has the length of  $2y + w_c$ , and way “2” has the length of  $2d_c + w_c$ . If  $y < d_c$ , way “1” is chosen. Thus, we assume that the magnetic charge appears at both tips of the crack and at the two walls with length of  $d_c$  from the tips, as shown in Fig. 4-11(b). So, equation (4-5) used to calculate the magnetic field is now changed to equation (4-7).

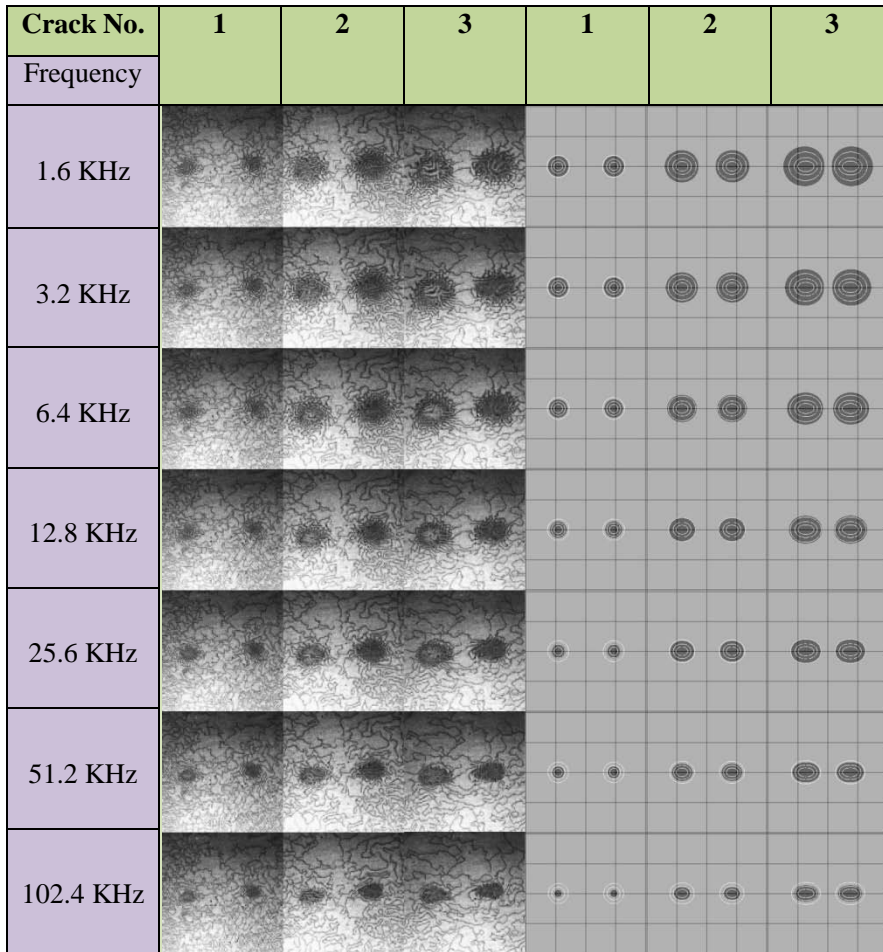
$$H_z = \left[ \frac{\xi}{4\pi\mu} \int_{-w_c/2}^{w_c/2} \int_{-d_c}^0 \frac{e^{\frac{z'}{\delta}(z-z')}}{\{(x-x')^2 + (y+lc/2)^2 + (z-z')^2\}^{3/2}} dz' dx' \right. \\ \left. - \frac{\xi}{4\pi\mu} \int_{-w_c/2}^{w_c/2} \int_{-d_c}^0 \frac{e^{\frac{z'}{\delta}(z-z')}}{\{(x-x')^2 + (y-lc/2)^2 + (z-z')^2\}^{3/2}} dz' dx' \right] \quad (4-7)$$

$$\begin{aligned}
& + \frac{\xi}{4\pi\mu} \int_{-\frac{l_c}{2}}^{-\frac{l_c}{2}+d_c} \int_{-d_c}^0 \frac{e^{\frac{z'}{\delta}}(z-z')}{\{(x+wc/2)^2+(y-y')^2+(z-z')^2\}^{3/2}} dz' dy' \\
& + \frac{\xi}{4\pi\mu} \int_{-\frac{l_c}{2}}^{-\frac{l_c}{2}+d_c} \int_{-d_c}^0 \frac{e^{\frac{z'}{\delta}}(z-z')}{\{(x-wc/2)^2+(y-y')^2+(z-z')^2\}^{3/2}} dz' dy' \\
& - \frac{\xi}{4\pi\mu} \int_{\frac{l_c}{2}-d_c}^{\frac{l_c}{2}} \int_{-d_c}^0 \frac{e^{\frac{z'}{\delta}}(z-z')}{\{(x+wc/2)^2+(y-y')^2+(z-z')^2\}^{3/2}} dz' dy' \\
& - \frac{\xi}{4\pi\mu} \int_{\frac{l_c}{2}-d_c}^{\frac{l_c}{2}} \int_{-d_c}^0 \frac{e^{\frac{z'}{\delta}}(z-z')}{\{(x-wc/2)^2+(y-y')^2+(z-z')^2\}^{3/2}} dz' dy' \Big]
\end{aligned}$$

#### 4.3.2. Results and discussion

Fig. 4-12 shows the experiment results and simulation results of the second suggestion. The specimens and cracks are the same as those of the first suggestion. The parameters for the simulation are the same as those in the Table 4-4 but the magnetic charge factor  $\xi = 2e - 5$ . The magnetic domain which is black color in Fig. 4-12(b), is similar with ellipse shape. This shape is similar with the experiment results. Furthermore, depending on the crack depth; the magnetic charges appearing on the crack wall are short or long in the direction of crack length ( $d_c$  distance). This is the reason that the crack with higher depth induces the magnetic domain with longer horizontal length as shown in both experiment results and simulation results. However, upon careful examination, one side of the magnetic domains in the experiment results, is smaller than the other. So, this method needs to be improved once more.





(a) Experiment results

(b) Simulation results

**Fig. 4-12** Results with the second suggestion

## 4.4. The third suggestion

### 4.4.1. Dipole model

As mentioned above, one side of the magnetic domains in the experiment results is smaller than the other. Therefore, we assume that the magnetic charges do not distribute equally on the wall of the crack ( $d_c$  distance). The eddy current starts to turn around the tips of the

crack at distance  $d_c$  from the tips. Thus, the eddy current is sparse far from the tips and highly concentrates at the tips of crack. It means that the magnetic charge factor  $\xi$  is not a constant value as shown in Fig. 4-13. We assume that  $\xi$  is linear along the wall of the crack,  $\xi = 0$  at  $y = \pm(l_c/2 - d_c)$ , and  $\xi = \pm\xi_0 = \text{constant}$  at  $y = \mp l_c/2$ . The  $m_{IC}$  can be described by equation (4-8) at the first half cycle and by the inverse sign at the second half cycle. Then magnetic field distribution can be calculated by substituting equation (4-8) into equation (4-7).

$$m_{IC} = \xi(y)e^{-\frac{t}{\delta}} \quad (4-8)$$

**Along the walls of crack:**

Right side of Eddy current:

$$\xi(y) = +\xi_0 \frac{-y - l_c/2 + d_c}{d}$$

Left side of Eddy current:

$$\xi(y) = -\xi_0 \frac{y - l_c/2 + d_c}{d}$$

**Two tips of crack:**

$$\xi(\pm l_c/2) = \mp \xi_0$$

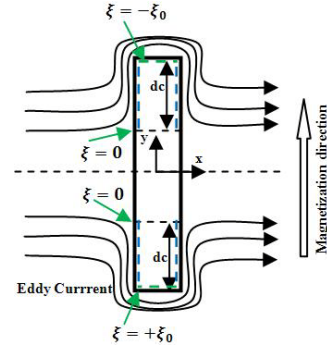
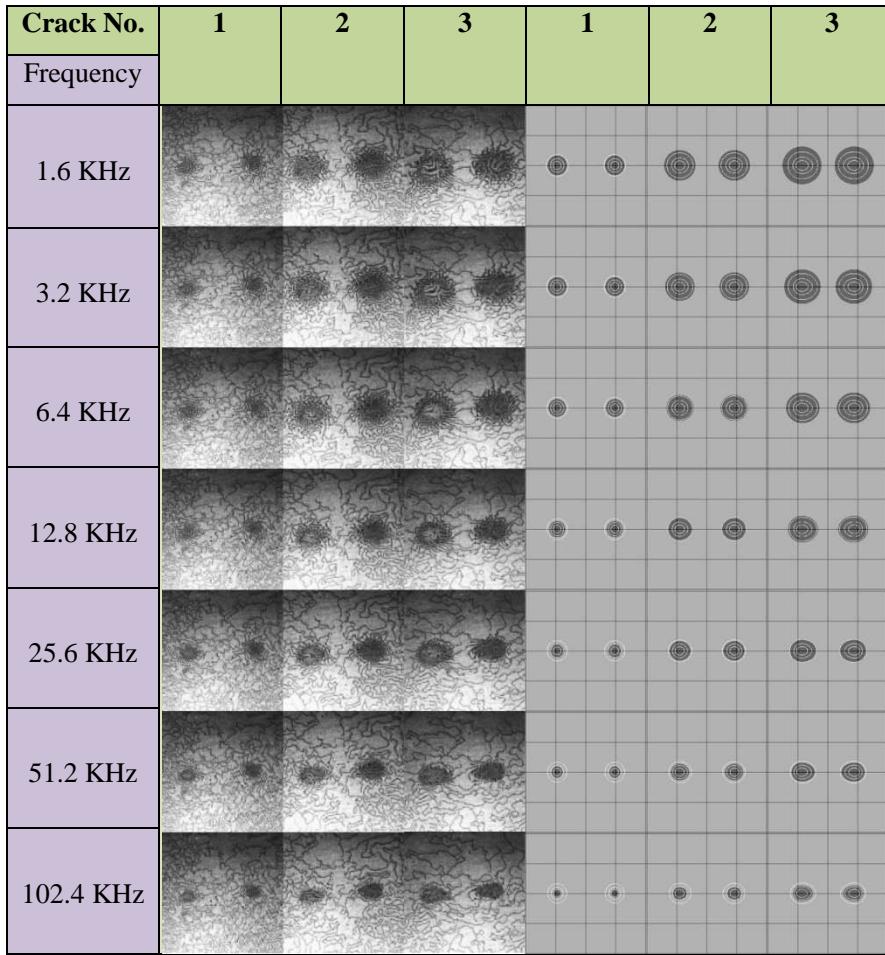


**Fig. 4-13** Eddy current flow – the third suggestion

**4.4.2. Results and discussion**

Fig. 4-14 shows the experiment and simulation results of the third suggestion. The specimens, cracks and the simulation parameters are the same as those of the first suggestion, but  $\xi_0 = 2.5e - 5$  is chosen. The magnetic domains tapered at one side, as in the experiment results. The simulation results were improved and became much similar with the experiment results.



(a) Experiment results

(b) Simulation results

**Fig. 4-14** Results with the third suggestion

## Chapter 5

### CONCLUSIONS

Numerical analysis software using a dipole model and a Magneto-Optical Film was used to simulate the distribution of the magnetic flux around cracks. The software allowed 3-D visualization of the magnetic distribution around a crack or multi-complex cracks on specimen of different shapes, sizes, positions and length directions. The Faraday effect in MOF was integrated into the dipole model in the software. Software supported user input of the properties of the MOF (saturated magnetic field  $H_s$ , bias magnetic field  $H_b$ , spatial resolution, image processing), the properties of the specimen (permeability  $\mu$ , electric conductivity  $\sigma$ ), frequency  $f$ , magnetic charge factor  $\xi$ , and the conditions of the experiment (temperature  $T$ , lift-off  $z$ ). The simulation of static magnetic field (horizontal magnetization and vertical magnetization) and alternative magnetic field. The software performance was determined by comparing the simulation results with the experiment results.

In the static magnetic field, the horizontal magnetization is induced by using yoke type magnetizer, were able to detect cracks except when the length of cracks are parallel with the magnetic direction. Otherwise, using cross type magnetizer to induce horizontal magnetization, the cracks can be detected all the direction of cracks. In the case of vertical magnetization, only the information of cracks are appeared, then the cracks can be detected without the effect of direction of cracks.

In the alternative magnetic field, the magnetic charges appeared at the two tips of the crack. Then, the magnetic domains appeared at the two tips of the crack with in a circle shapes. The magnetic charges appeared equally at the two tips and at the walls of distance  $dc$  from the tips of the crack. Then, the magnetic domains appeared similar as ellipse shapes. The magnetic charges appeared linearly at the walls and constantly at the tips of the cracks. Then, the magnetic domains appeared as oblate shapes and taper on one side. This suggestion gave the best results.

## REFERENCES

1. Wei Dong, Zhou Zhenggan, Ni Xiansheng, "Application of linear frequency modulation pulse compression in air-coupled ultrasonic testing", ICACC 2010, Vol. 2, pp. 53 – 57.
2. Y. Ito, T. Masuda, K. Nagao, K. Matsuoka, "Ultrasonic testing system for ERW mill", IAS '97, Vol. 2, pp. 866 – 872.
3. Liu Guimin, Yong Qingsong, Li Bin, "Experiments on the Ultrasonic Testing of the Austenitic Dissimilar Welding Joint of Steel Type 22SiMn2TiB", ICMTMA 2011, Vol. 2, pp. 156 – 159.
4. Zhou Runjing, Zhang Fei, "Application of Ultrasonic for Pipeline Flaw Detection", ICEMI '07, pp. 4-472 - 4-475.
5. V. Nagarkar, J. Gordon, S. Vasile, P. Gothoskar, F. Hopkins, "High resolution X-ray sensor for non destructive evaluation", Nuclear Science Symposium and Medical Imaging Conference Record 1996, Vol. 43, pp. 1559 - 1563.
6. X. Wang, B. Wong, K. Khoo, C. Tui, F. Foo, "Image Enhancement for Radiographic Non-Destructive Inspection of the Aircraft", APCNDT 2006.
7. J. Xu, T. LIU, B. Wong , S. Hassan, "Automatic X-ray Crack Inspection for Aircraft Wing Fastener Holes", AeroNDT 2010.
8. X. Wang, B. Wong, C. Tui, "Real-time Radiographic Non-destructive Inspection for Aircraft Maintenance", WCNDT 2008.
9. G. L. Fitzpatrick, D. K. Thome, R. L. Skaugset, W. C. L. Shih, and E.Y. C. Shih, "Aircraft inspection with the magneto-optic/eddy current imager", Can. Natl.NDT Mag. 1994, vol. 15, no. 2, pp. 13–30.
10. J. Lee, J. Hwang, J. Jun, "Inspection of Cracks on the Express Train Wheel Using a High Speed Scan Type Magnetic Camera", KSME 2008c, pp. 31-36.

11. J. Lee, J. Hwang, J. Jun, S. Choi, "Nondestructive Testing and Crack Evaluation of Ferromagnetic Material by Using the Linearly Integrated Hall Sensor Array", JMST 2008, Vol. 22, pp. 2310-2317.
12. J. Jun, J. Lee, "Nondestructive Evaluation of a Crack on Austenitic Stainless Steel Using the Sheet Type Induced Current and the Hall Sensor Array", JMST 2008, Vol. 22, No. 9, pp. 1684-1691.
13. T. VETTERLEIN, S. GEORGI, TIEDE, M. WAGENER, H. RONGEN, "Automated Dye Penetrant Systems with Process Control and Documentation in the Aerospace Industry" ECNDT 2006 - Mo.2.1.2.
14. N. P. Migoun, A. B. Gnusin, M. Stadthaus, G. R. Jaenisch, "New Potentials of Penetrant Testing", ECNDT 2006 - Th.1.8.1.
15. Brian Larson, "Study of the Factors Affecting the Sensitivity of Liquid Penetrant Inspections: Review of Literature Published from 1970 to 1998", DOT/FAA/AR-01/95, 1/2002.
16. K. Kosmas, Ch. Sargentis, D. Tsamakias, E. Hristoforou, Non-destructive evaluation of magnetic metallic materials using Hall Sensors, Journal of Materials Technology 161 (2005) 359-392.
17. J. Jun, J. Hwang, J. Lee, Quantitative Nondestructive Evaluation of the Crack on the Austenite Stainless Steel Using the Induced Eddy Current and the Hall Sensor Array, IMTC 2007.
18. Jin Tao, Que Peiwen, Tao Zhengsu, Development of magnetic flux leakage pipe inspection robot using Hall sensors, IEEE 2004 pp.325-329.
19. Johannes Atzlesberger, Bernhard Zagar, Magnetic flux leakage measurement setup for defect detection, Procedia Engineering 5 (2010) 1401-1404.
20. S. Obeid, T. Dogaru, F. Tranjan, Rotational GMR magnetic sensor based eddy current probes for detecting buried corner cracks at the edge of holes in metallic structures, IEEE 2008.

21. Kataoka, Y., Wakiwaka, H., Shinoura, O., Leakage flux testing using a GMR line sensor and the rotating magnetic field, IEEE Vol.2 (2002) pp. 800-803.
22. T. Numata, et al., "Magneto-optical leakage flux testing of steel", IEEE Transactions on Magnetics 1989, Vol. 25 , Is. 5.
23. Li Bo, Wang Xiangfeng, Yang Hongping, Zhou Zhenliu, "Aircraft Rivets Defect Recognition Method Based on Magneto-optical Images", MVHI 2010, pp. 788 – 791.
24. Gao Qing-ji, Jing Ming-lan, "Image-Processing Algorithms of Magneto-Optic Imaging for Aircraft Multi-Skin Inspection", ICMT 2010, pp. 1 – 5.
25. J. Lee, J. Hwang, T. Shoji, J. Lim, Modeling of characteristics of Magneto-optical sensor using FEM and Dipole Model for Nondestructive Evaluation, Key Engineering Materials Vols.297-300 (2005) pp.2022-2027.
26. Zhang Guoguang, Liu Jing, "Finite Element Modelling of Circumferential Magnetic Flux Leakage Inspection in Pipeline", ICICTA 2010, Vol. 2, pp. 327 – 330.
27. T. Miyoshi, G. Maeda, "Finite element analysis of leakage magnetic flux from an induction heating system", IEEE Transactions on Magnetics, Vol. 18 , Is. 3, pp. 917 – 920.
28. N. Harfield, J. R. Bowler, Theory of thin-skin eddy-current interaction with the surface of cracks. IEEE Vol. 82, No. 9, pp. 4590 – 4603, 06/2009.
29. Z. Badics, et al., An effective 3-D element scheme for computing electromagnetic field distortions due to defects in eddy-current nondestructive evaluation, IEEE transaction on magnetic, Vol. 33, No. 02, 03/1997.
30. M. Dutta, H. Ghorbel, K. Stanley, Dipole modeling of magnetic flux leakage, IEEE Vol.45, No.4, 2009.
31. M. Abd Elnaby, I. Elshafiey, S. Khamees, S. Serag-Eldeen, "Finite element computational modeling of magneto-optic imaging", Microelectronics, The 14th International Conference on 2002 – ICM 2002.

32. S. Lee, S. Song, D. Jiles, H. Hauser, "Magneto-optic sensor for remote evaluation of surfaces", *IEEE transaction on magnetic* 2005, Vol. 41 , Is. 7.
33. J. Lee, S. Lyu, Y. Nam, An algorithm for the characterization of surface crack by use of dipole model and magneto-optic Non-Destructive inspection system.
34. D. Minkov, J. Lee, T. Shoji, Improvement of the Dipole Model of a Surface Crack, *Material Evaluation*, Vol. 58, No. 5, pp. 661-666.
35. J. Lee, T. Shoji, D. Minkov and M. Ishihara, Novel NDI by use of Magneto-Optical Film, *Journal of The Japan Society of Mechanical Engineers[A]*, [No.97-0580] (1997), in press.
36. J. Lee, T. Shoji, Development of a Novel NDI System by use of Magneto-Optical Film, *Proceedings of JSNDI Spring Conference* (1997) pp. 185-188.
37. M. Ishihara, T. Sakamoto, K. Haruna, N. Nakamura, K. Machida, Y. Asahara, Advanced Magnetic Flux Leakage Testing System using Magneto-Optical Film, *The Japanese Society for Non-Destructive Inspection*, 45(4) (1996) pp.283-289.
38. G.L. Fitzpatrick, D.K. Thome, R.L. Skaugset , E.Y.C. Shih, W.C.L. Shih, Magneto-optical/ Eddy current imaging of aging aircraft-A New NDI Technique, *Material Evaluation*, Vol. 51, No. 12, pp. 1402~1407.
39. J. Lee et al., Non-destructive testing in the high-temperature regime by using a magneto-optical film, *NDT&E International* 41(2008) 420-426.
40. J. Lee, T. Shoji, D. Seo, Theoretical consideration of nondestructive testing by use of vertical magnetization and magneto-optical sensor, *KSME Int J* Vol.18 No. 4, pp 640~648, 2004.
41. J. Kim, M. Choi, J. Lee, "Employing magnetic sensor array for inspecting cracks in a pipeline", *Sensors Applications Symposium (SAS)*, 2011 IEEE, pp. 273 – 276.
42. J. Lee, J. Hwang, S. Choi, A study of the quantitative nondestructive evaluation using the cross type magnetic source and the magnetic camera, *KEM Vols.* 321-323 (2006), pp 1447-1450.



43. J. Lee, J. Jun, J. Hwang, S. Lee, Development of numerical analysis software for the NDE by using dipole model, Key Eng Mat Vols. 353-358 (2007) pp. 2382-2386.
44. Y. Deng at al., Characterization of magneto-optic imaging data for aircraft inspection, IEEE Vol. 42, No. 10, 11/2006.
45. David K. Thome, Development of an improved magneto-optic/eddy-current imager, NTIS, Springfield, Virginia.

## **ACKNOWLEDGEMENT**

I would like to express my gratitude to my advisor, Prof. Jinyi Lee at Department of Control, Instrumentation and Robot Engineering for his supports. That he willingly shared the knowledge with me during the research and writing of my thesis. His advices are always very helpful in both doing research and living in Korea.

I would also like to thanks to Prof. Jongwoo Jun, Prof. Chang-Hyun Cho, Prof. N. Ko, Prof. S. Pan and all professors at Department of Control, Instrumentation and Robot Engineering for teaching me the knowledge.

I like to thanks to my lab-mates of Research Center for Real Time-NDT Chosun University for 2 years of my studying and living in Korea: Dr. Jiseong Hwang, Dr. Jungmin Kim, Mr. Jaesun Lee, Mr. Youngmin Park, Mr. Hoyoun Choi, Mr. Myungki Choi, Ms. Hyunjung Kim, Mr. Taesuk Kim, and Ms. Minja Kim.

I am extremely thankful to my parents, all my family and friends for their love, support, and encouragement in every moment of my life. From my heart, I always wish and pray for them.

Le Minh Huy

# 저작물 이용 허락서

학 과	제어계측공학과	학 번	20097749	과 정	석사
성 명	한글 레민후이 한문 영문 LE MINH HUY				
주 소	광주시 동구 지산동 504-8				
연락처	e-mail : kebitmat_f@yahoo.com				
논문제목	한글:자기광학 비파괴검사의 시뮬레이션				
	영문: <b>Simulation of Magneto-Optical Nondestructive Testing</b>				

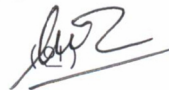
본인이 저작한 위의 저작물에 대하여 다음과 같은 조건 아래 조선대학교가 저작물을 이용할 수 있도록 허락하고 동의합니다.

- 다 음 -

1. 저작물의 DB 구축 및 인터넷을 포함한 정보통신망에의 공개를 위한 저작물의 복제, 기억장치에의 저장, 전송 등을 허락함
2. 위의 목적을 위하여 필요한 범위 내에서의 편집과 형식상의 변경을 허락함(다만, 저작물의 내용변경은 금지함)
3. 배포·전송된 저작물의 영리적 목적을 위한 복제, 저장, 전송 등은 금지함
4. 저작물에 대한 이용기간은 5 년으로 하고, 기간종료 3 개월 이내에 별도의 의사 표시가 없을 경우에는 저작물의 이용기간을 계속 연장함
5. 해당 저작물의 저작권을 타인에게 양도하거나 출판을 허락을 하였을 경우에는 1 개월 이내에 대학에 이를 통보함
6. 조선대학교는 저작물 이용의 허락 이후 해당 저작물로 인하여 발생하는 타인에 의한 권리 침해에 대하여 일체의 법적 책임을 지지 않음
7. 소속 대학의 협정기관에 저작물의 제공 및 인터넷 등 정보통신망을 이용한 저작물의 전송·출력을 허락함

동의여부 : 동의(○) 반대( )

2011년 8월 25일 Le Minh Huy



조선대학교 총장 귀하